

6 Tomographic Imaging with Diffracting Sources

Diffraction tomography is an important alternative to straight ray tomography. For some applications, the harm caused by the use of x-rays, an ionizing radiation, could outweigh any benefits that might be gained from the tomogram. This is one reason for the interest in imaging with acoustic or electromagnetic radiation, which are considered safe at low levels. In addition, these modalities measure the acoustic and electromagnetic refractive index and thus make available information that isn't obtainable from x-ray tomography.

As mentioned in Chapter 4, the accuracy of tomography using acoustic or electromagnetic energy and straight ray assumptions suffers from the effects of refraction and/or diffraction. These cause each projection to not represent integrals along straight lines but, in some cases where geometrical laws of propagation apply, paths determined by the refractive index of the object. When the geometrical laws of propagation don't apply, one can't even use the concept of line integrals—as will be clear from the discussions in this chapter.

There are two approaches to correcting these errors. One approach is to use an initial estimate of the refractive index to estimate the path each ray follows. This approach is known as algebraic reconstruction and, for weakly refracting objects, will converge to the correct refractive index distribution after a few iterations. We will discuss algebraic techniques in Chapter 7.

When the sizes of inhomogeneities in the object become comparable to or smaller than a wavelength, it is not possible to use ray theory (geometric propagation) based concepts; instead one must resort directly to wave propagation and diffraction based phenomena. In this chapter, we will show that if the interaction of an object and a field is modeled with the wave equation, then a tomographic reconstruction approach based on the Fourier Diffraction Theorem is possible for weakly diffracting objects. The Fourier Diffraction Theorem is very similar to the Fourier Slice Theorem of conventional tomography: In conventional (or straight ray) tomography, the Fourier Slice Theorem says that the Fourier transform of a projection gives the values of the Fourier transform of the object along a straight line. When diffraction effects are included, the Fourier Diffraction Theorem says that a “projection” yields the Fourier transform of the object over a semicircular arc. This result is fundamental to diffraction tomography.

In this chapter the basics of diffraction tomography are presented for application with acoustic, microwave, and optical energy. For each case we

will start with the wave equation and use either the Born or the Rytov approximation to derive a simple expression that relates the scattered field to the object. This relationship will then be inverted for several measurement geometries to give an estimate of the object as a function of the scattered field. Finally, we will show simulations and experimental results that show the limitations of the method.

6.1 Diffracted Projections

Tomography with diffracting energy requires an entirely different approach to the manner in which projections are mathematically modeled. Acoustic and electromagnetic waves don't travel along straight rays and the projections aren't line integrals, so we will describe the flow of energy with a wave equation.

We will first consider the propagation of waves in homogeneous media, although our ultimate interest lies in imaging the inhomogeneities within an object. The propagation of waves in a homogeneous object is described by a wave equation, which is a second-order linear differential equation. Given such an equation and the "source" fields in an aperture, we can determine the fields everywhere else in the homogeneous medium.

There are no direct methods for solving the problem of wave propagation in an inhomogeneous medium; in practice, approximate formalisms are used that allow the theory of homogeneous medium wave propagation to be used for generating solutions in the presence of weak inhomogeneities. The better known among these approximate methods go under the names of Born and Rytov approximations.

Although in most cases we are interested in reconstructing three-dimensional objects, the diffraction tomography theory presented in this chapter will deal mostly with the two-dimensional case. Note that when a three-dimensional object can be assumed to vary only slowly along one of the dimensions, a two-dimensional theory can be readily applied to such an object. This assumption, for example, is often made in conventional computerized tomography where images are made of single slices of the object. In any case, we have two reasons for limiting our presentation to the two-dimensional case: First and most importantly, the ideas behind the theory are often easier to visualize (and certainly to draw) in two dimensions. Second, the technology has not yet made it practical to implement large three-dimensional transforms that are required for direct three-dimensional reconstructions of objects; furthermore, direct display of three-dimensional entities isn't easy.

6.1.1 Homogeneous Wave Equation

An acoustic pressure field or an electromagnetic field must satisfy the following differential equation [Goo68]:

$$\nabla^2 u(\vec{r}, t) - \frac{1}{c^2} \frac{\nabla^2}{dt^2} u(\vec{r}, t) = 0 \quad (1)$$

where u represents the magnitude of the field as a function of position \vec{r} and time t and c is the velocity of the field as a function of position.

This form of the wave equation is more complicated than needed; most derivations of diffraction tomography are done by considering only one temporal frequency at a time. This decomposition can be accomplished by finding the Fourier transform of the field with respect to time at each position \vec{r} . Note that the above differential equation is linear so that the solutions for different frequencies can be added to find additional solutions.

A field $u(\vec{r}, t)$ with a temporal frequency of ω radians per second (rps) satisfies the equation

$$[\nabla^2 + k^2(\vec{r})]u(\vec{r}, t) = 0 \quad (2)$$

where $k(\vec{r})$ is the wavenumber of the field and is equal to

$$k(\vec{r}) = \frac{2\pi}{\lambda} = \frac{2\pi\omega}{c} \quad (3)$$

where λ is the field's wavelength. At this point the field is at a single frequency and we will write it as

$$\text{Real Part } \{u(\vec{r})e^{-j\omega t}\}. \quad (4)$$

In this form it is easy to see that the time dependence of the field can be suppressed and the wave equation rewritten as

$$(\nabla^2 + k^2(\vec{r}))u(\vec{r}) = 0. \quad (5)$$

For acoustic (or ultrasonic) tomography, $u(\vec{r})$ can be the pressure field at position \vec{r} . For the electromagnetic case, assuming the applicability of a scalar propagation equation, $u(\vec{r})$ may be set equal to the complex amplitude of the electric field along its polarization. In both cases, $u(\vec{r})$ represents the complex amplitude of the field.

For homogeneous media the wavenumber is constant and we can further simplify the wave equation. Setting the wavenumber equal to

$$k(\vec{r}) = k_0 \quad (6)$$

the wave equation becomes

$$(\nabla^2 + k_0^2)u(\vec{r}) = 0. \quad (7)$$

The vector gradient operator, ∇ , can be expanded into its two-dimensional representation and the wave equation becomes

$$\frac{\partial^2 u(\vec{r})}{\partial x^2} + \frac{\partial^2 u(\vec{r})}{\partial y^2} + k_0^2 u(\vec{r}) = 0. \quad (8)$$

As a trial solution we let

$$u(\vec{r}) = e^{j\vec{k} \cdot \vec{r}} \quad (9)$$

where the vector $\vec{k} = (k_x, k_y)$ is the two-dimensional propagation vector and $u(\vec{r})$ represents a two-dimensional plane wave of spatial frequency $|\vec{k}|$. This form of $u(\vec{r})$ represents the basis function for the two-dimensional Fourier transform; using it, we can represent any two-dimensional function as a weighted sum of plane waves. Calculating the derivatives as indicated in (8), we find that only plane waves that satisfy the condition

$$|\vec{k}|^2 = k_x^2 + k_y^2 = k_0^2 \quad (10)$$

satisfy the wave equation. This condition is consistent with our intuitive picture of a wave and our earlier description of the wave equation, since for any frequency wave only a single wavelength can exist no matter in which direction the wave propagates.

The homogeneous wave equation is a linear differential equation so we can write the general solution as a weighted sum of each possible plane wave solution. In two dimensions, at a temporal frequency of ω , the field $u(\vec{r})$ is given by

$$u(\vec{r}) = \frac{1}{2\pi} \int_{-\infty}^{\infty} \alpha(k_y) e^{j(k_x x + k_y y)} dk_y + \frac{1}{2\pi} \int_{-\infty}^{\infty} \beta(k_y) e^{j(-k_x x + k_y y)} dk_y \quad (11)$$

where by (10)

$$k_x = \sqrt{k_0^2 - k_y^2}. \quad (12)$$

The form of this equation might be surprising to the reader for two reasons. First we have split the integral into two parts. We have chosen to represent the coefficients of waves traveling to the right by $\alpha(k_y)$ and those of waves traveling to the left by $\beta(k_y)$. In addition, we have set the limits of the integrals to go from $-\infty$ to ∞ . For k_y^2 greater than k_0^2 , the radical in (12) becomes imaginary and the plane wave becomes an evanescent wave. These are valid solutions to the wave equation, but because k_y is imaginary, the exponential has a real or attenuating component. This real component causes the amplitude of the wave to either grow or decay exponentially. In practice, these evanescent waves only occur to satisfy boundary conditions, always decaying rapidly far from the boundary, and can often be ignored at a distance greater than 10λ from an inhomogeneity.

We will now show by using the plane wave representation that it is possible to express the field anywhere in terms of the fields along a line. The three-dimensional version of this idea gives us the field in three-space if we know the field at all points on a plane.

Consider a source of plane waves to the left of a vertical line as shown in Fig. 6.1. If we take the one-dimensional Fourier transform of the field along

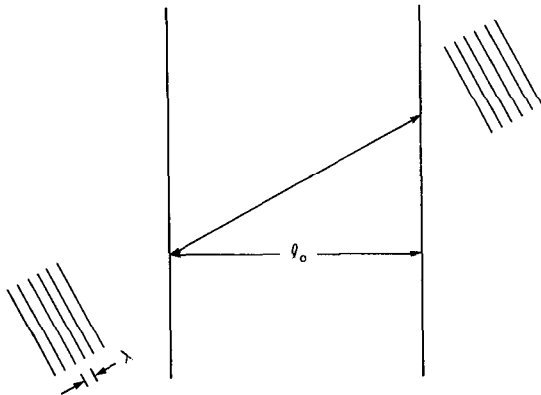


Fig. 6.1: A plane wave propagating between two planes undergoes a phase shift dependent on the distance between the planes and the direction of the plane wave.

the vertical line, we can decompose the field into a number of one-dimensional components. Each of these one-dimensional components can then be attributed to one of the valid plane wave solutions to the homogeneous wave equation, because for any one spatial frequency component, k_y , there can exist only two plane waves that satisfy the wave equation. Since we have already constrained the incident field to propagate to the right (all sources are to the left of the measurement line), a one-dimensional Fourier component at a frequency of k_y , can be attributed to a two-dimensional wave with a propagation vector of $(\sqrt{k_0^2 - k_y^2}, k_y)$.

We can put this on a more mathematical basis if we compare the one-dimensional Fourier transform of the field to the general form of the wave equation. If we ignore waves that are traveling to the left, then the general solution to the wave equation becomes

$$u(\vec{r}) = \frac{1}{2\pi} \int_{-\infty}^{\infty} \alpha(k_y) e^{j(k_x x + k_y y)} dk_y. \quad (13)$$

If we also move the coordinate system so that the measurement line is at $x = 0$, the expression for the field becomes equal to the one-dimensional Fourier transform of the amplitude distribution function $\alpha(k_y)$.

$$u(0, y) = \frac{1}{2\pi} \int_{-\infty}^{\infty} \alpha(k_y) e^{jk_y y} dk_y. \quad (14)$$

If we invert the transform relationship, this equation tells us that the amplitude distribution function can be obtained from the fields on the line $x = 0$ by

$$\alpha(k_y) = \text{Fourier transform of } \{u(0, y)\}. \quad (15)$$

This amplitude distribution function can then be substituted into the equation for $u(\vec{r})$ to obtain the fields everywhere right of the line $x = 0$.

We will now show how it is possible to relate fields on two parallel lines. Again consider the situation diagrammed in Fig. 6.1. If we know a priori that all the sources for the field are positioned, for example, to the left of the line at $x = l_0$, then we can decompose the field $u(x = l_0, y)$ into its plane wave components. Given a plane wave $u_{\text{plane wave}}(x = l_0, y) = \alpha e^{j(k_x l_0 + k_y y)}$ the field undergoes a phase shift as it propagates to the line $x = l_1$, and we can write

$$u_{\text{plane wave}}(x = l_1, y) = \alpha e^{j(k_x l_0 + k_y y)} e^{j k_x (l_1 - l_0)} = u_{\text{plane wave}}(x = l_0, y) e^{j k_x (l_1 - l_0)}. \quad (16)$$

Thus the complex amplitude of the plane wave at $x = l_1$ is related to its complex amplitude at $x = l_0$ by a factor of $e^{j k_x (l_1 - l_0)}$.

The complete process of finding the field at a line $x = l_1$ follows in three steps:

- 1) Take the Fourier transform of $u(x = l_0, y)$ to find the Fourier decomposition of u as a function of k_y .
- 2) Propagate each plane wave to the line $x = l_1$ by multiplying its complex amplitude by the phase factor $e^{j k_x (l_1 - l_0)}$ where, as before, $k_x = \sqrt{k_0^2 - k_y^2}$.
- 3) Find the inverse Fourier transform of the plane wave decomposition to find the field at $u(x = l_1, y)$.

These steps can be reversed if, for some reason, one wished to implement on a computer the notion of backward propagation; more on that subject later.

6.1.2 Inhomogeneous Wave Equation

For imaging purposes, our main interest lies in inhomogeneous media. We, therefore, write a more general form of the wave equation as

$$[\nabla^2 + k(\vec{r})^2]u(\vec{r}) = 0. \quad (17)$$

For the electromagnetic case, if we ignore the effects of polarization we can consider $k(\vec{r})$ to be a scalar function representing the refractive index of the medium. We now write

$$k(\vec{r}) = k_0 n(\vec{r}) = k_0 [1 + n_\delta(\vec{r})] \quad (18)$$

where k_0 represents the average wavenumber of the medium and $n_\delta(\vec{r})$ represents the refractive index deviations. In general, we will assume that the object has a finite size and therefore $n_\delta(\vec{r})$ is zero outside the object. Rewriting the wave equation we find

$$(\nabla^2 + k_0^2)u(\vec{r}) = -k_0^2[n(\vec{r})^2 - 1](\vec{r})u(\vec{r}) \quad (19)$$

where $n(\vec{r})$ is the electromagnetic refractive index of the media and is given

by

$$n(\vec{r}) = \sqrt{\frac{\mu(\vec{r})\epsilon(\vec{r})}{\mu_0\epsilon_0}}. \quad (20)$$

Here we have used μ and ϵ to represent the magnetic permeability and dielectric constant and the subscript zero to indicate their average values. This new term, on the right-hand side of (19), is known as a forcing function for the differential equation $(\nabla^2 + k_0^2)u(\vec{r})$.

Note that (19) is a *scalar* wave propagation equation. Its use implies that there is no depolarization as the electromagnetic wave propagates through the medium. It is known [Ish78] that the depolarization effects can be ignored only if the wavelength is much smaller than the correlation size of the inhomogeneities in the object. If this condition isn't satisfied, then strictly speaking we must use the following vector wave propagation equation:

$$\nabla^2 \vec{E}(rv) + k_0^2 n^2 \vec{E}(\vec{r}) - 2\nabla \left[\frac{\nabla n}{n} \cdot \vec{E} \right] = 0 \quad (21)$$

where \vec{E} is the electric field vector. A vector theory for diffraction tomography based on this equation has yet to be developed.

For the acoustic case, first-order approximations give us the following wave equation [Kak85], [Mor68]:

$$(\nabla^2 + k_0^2)u(\vec{r}) = -k_0^2[n^2(\vec{r}) - 1]u(\vec{r}) \quad (22)$$

where n is the *complex refractive index* at position \vec{r} , and is equal to

$$n(\vec{r}) = \frac{c_0}{c(\vec{r})} \quad (23)$$

where c_0 is the propagation velocity in the medium in which the object is immersed and $c(\vec{r})$ is the propagation velocity at location \vec{r} in the object. For the acoustic case where only compressional waves in a viscous compressible fluid are involved, we have

$$c(\vec{r}) = \frac{1}{\sqrt{\rho(\vec{r})\kappa(\vec{r})}} \quad (24)$$

where ρ and κ are the *local density* and the *complex compressibility* at location \vec{r} .

The forcing function in (22) is only valid provided we can ignore the first and higher order derivatives of the medium parameters. If these higher order derivatives can't be ignored, the exact form for the wave equation must be used:

$$(\nabla^2 + k_0^2)u(\vec{r}) = k_0^2\gamma_\kappa u - \nabla \cdot (\gamma_\rho \nabla u) \quad (25)$$

where

$$\gamma_k = \frac{K - K_0}{K_0} \quad (26)$$

$$\gamma_\rho = \frac{\rho - \rho_0}{\rho}. \quad (27)$$

κ_0 and ρ_0 are either the compressibility and the density of the medium in which the object is immersed, or the average compressibility and the density of the object, depending upon how the process of imaging is modeled. On the other hand, if the object is a solid and can be modeled as a linear isotropic viscoelastic medium, the forcing function possesses another more complicated form. Since this form involves tensor notation, it will not be presented here and the interested reader is referred to [Iwa75].

Due to the similarities of the electromagnetic and acoustic wave equations, a general form of the wave equation for the small perturbation case can be written as

$$(\nabla^2 + k_0^2)u(\vec{r}) = -o(\vec{r})u(\vec{r}) \quad (28)$$

where

$$o(\vec{r}) = k_0^2[n^2(\vec{r}) - 1]. \quad (29)$$

This allows us to describe the math involved in diffraction tomography independent of the form of energy used to illuminate the object.

We will consider the field, $u(\vec{r})$, to be the sum of two components, $u_0(\vec{r})$ and $u_s(\vec{r})$. The component $u_0(\vec{r})$, known as the incident field, is the field present without any inhomogeneities, or, equivalently, a solution to the equation

$$(\nabla^2 + k_0^2)u_0(\vec{r}) = 0. \quad (30)$$

The component $u_s(\vec{r})$, known as the scattered field, will be that part of the total field that can be attributed solely to the inhomogeneities. What we are saying is that with $u_0(\vec{r})$ as the solution to the above equation, we want the field $u(\vec{r})$ to be given by $u(\vec{r}) = u_0(\vec{r}) + u_s(\vec{r})$. Substituting the wave equation for u_0 and the sum representation for u into (28), we get the following wave equation for just the scattered component:

$$(\nabla^2 + k_0^2)u_s(\vec{r}) = -u(\vec{r})o(\vec{r}). \quad (31)$$

The scalar Helmholtz equation (31) can't be solved for $u_s(\vec{r})$ directly, but a solution can be written in terms of the Green's function [Mor53]. The Green's function, which is a solution of the differential equation

$$(\nabla^2 + k_0^2)g(\vec{r}|\vec{r}') = -\delta(\vec{r} - \vec{r}'), \quad (32)$$

is written in three-space as

$$g(\vec{r}|\vec{r}') = \frac{e^{jk_0 R}}{4\pi R} \quad (33)$$

with

$$R = |\vec{r} - \vec{r}'|. \quad (34)$$

In two dimensions the solution of (32) is written in terms of a zero-order Hankel function of the first kind, and can be expressed as

$$g(\vec{r}'|\vec{r}') = \frac{j}{4} H_0^{(1)}(k_0 R). \quad (35)$$

In both cases, the Green's function, $g(\vec{r}|\vec{r}')$, is only a function of the difference $\vec{r} - \vec{r}'$ so we will often represent the function as simply $g(\vec{r} - \vec{r}')$. Because the object function in (32) represents a point inhomogeneity, the Green's function can be considered to represent the field resulting from a single point scatterer.

It is possible to represent the forcing function of the wave equation as an array of impulses or

$$o(\vec{r})u(\vec{r}) = \int o(\vec{r}')u(\vec{r}')\delta(\vec{r} - \vec{r}') d\vec{r}'. \quad (36)$$

In this equation we have represented the forcing function of the inhomogeneous wave equation as a summation of impulses weighted by $o(\vec{r})u(\vec{r})$ and shifted by \vec{r} . The Green's function represents the solution of the wave equation for a single delta function; because the left-hand side of the wave equation is linear, we can write a solution by summing up the scattered field due to each individual point scatterer.

Using this idea, the total field due to the impulse $o(\vec{r}')u(\vec{r}')\delta(\vec{r} - \vec{r}')$ is written as a summation of scaled and shifted versions of the impulse response, $g(\vec{r})$. This is a simple convolution and the total radiation from all sources on the right-hand side of (31) must be given by the following superposition:

$$u_s(\vec{r}) = \int g(\vec{r} - \vec{r}')o(\vec{r}')u(\vec{r}') d\vec{r}'. \quad (37)$$

At first glance it might appear that this is the solution we need for the scattered field, but it is not that simple. We have written an integral equation for the scattered field, u_s , in terms of the total field, $u = u_0 + u_s$. We still need to solve this equation for the scattered field and we will now discuss two approximations that allow this to be done.

6.2 Approximations to the Wave Equation

In the last section we derived an inhomogeneous integral equation to represent the scattered field, $u_s(\vec{r})$, as a function of the object, $o(\vec{r})$. This

equation can't be solved directly, but a solution can be written using either of the two approximations to be described here. These approximations, the Born and the Rytov, are valid under different conditions but the form of the resulting solutions is quite similar. These approximations are the basis of the Fourier Diffraction Theorem.

Mathematically speaking, (37) is a Fredholm equation of the second kind. A number of mathematicians have presented works describing the solution of scattering integrals [Hoc73], [Col83] which should be consulted for the theory behind the approximations we will present.

6.2.1 The First Born Approximation

The first Born approximation is the simpler of the two approaches. Recall that the total field, $u(\vec{r})$, is expressed as the sum of the incident field, $u_0(\vec{r})$, and a small perturbation, $u_s(\vec{r})$, or

$$u(\vec{r}) = u_0(\vec{r}) + u_s(\vec{r}). \quad (38)$$

The integral of (37) is now written as

$$u_s(\vec{r}) = \int g(\vec{r} - \vec{r}') o(\vec{r}') u_0(\vec{r}') d\vec{r}' + \int g(\vec{r} - \vec{r}') o(\vec{r}') u_s(\vec{r}') d\vec{r}' \quad (39)$$

but if the scattered field, $u_s(\vec{r})$, is small compared to $u_0(\vec{r})$ the effects of the second integral can be ignored to arrive at the approximation

$$u_s(\vec{r}) \approx u_B(\vec{r}) = \int g(\vec{r} - \vec{r}') o(\vec{r}') u_0(\vec{r}') d\vec{r}'. \quad (40)$$

An even better estimate can be found by substituting $u_0(\vec{r}) + u_B(\vec{r})$ for $u_0(\vec{r})$ in (40) to find

$$u_B^{(2)}(\vec{r}) = \int g(\vec{r} - \vec{r}') o(\vec{r}') [u_0(\vec{r}') + u_B(\vec{r}')] d\vec{r}'. \quad (41)$$

In general, the i th-order Born field can be written

$$u_B^{(i+1)}(\vec{r}) = \int g(\vec{r} - \vec{r}') o(\vec{r}') [u_0(\vec{r}') + u_B^{(i)}(\vec{r}')] d\vec{r}'. \quad (42)$$

An alternate representation is possible if we write

$$u(\vec{r}) = u_0(\vec{r}) + u_1(\vec{r}) + u_2(\vec{r}) + \dots \quad (43)$$

where

$$u_{(i+1)}(\vec{r}) = \int u_i(\vec{r}') o(\vec{r}') g(\vec{r} - \vec{r}') d\vec{r}'. \quad (44)$$

By expanding (42) it is possible to see that an approximate expression for the

scattered field, $u_B^{(i)}$, is

$$u_B^{(i)}(\vec{r}) = \sum_{j=0}^i u_j(\vec{r}) \quad (45)$$

and in the limit

$$u(\vec{r}) \approx u_0(\vec{r}) + u_1(\vec{r}) + u_2(\vec{r}) + u_3(\vec{r}) + \dots \quad (46)$$

This representation (46) has a more intuitive interpretation. The Green's function gives the scattered field due to a point scatterer and thus the integral of (42) can be interpreted as calculating the first-order scattered field due to the field u_i . For this reason the first-order Born approximation represents the first-order scattered field and u_i represents the i th-order scattered field.

The result can also be interpreted in terms of the Huygens principle; each point in the object produces a scattered field proportional to the scattering potential at the site of the scatterer. Each of these partial scattered fields interacts with the other scattering centers in the object and if the Born series converges the total field is the sum of the partial scattered fields.

While the higher order Born series does provide a good model of the scattering process, reconstruction algorithms based on this series have yet to be developed. These algorithms are currently being researched; in the meantime, we will study reconstruction algorithms based on first-order approximations [Bar78], [Sla85].

The first Born approximation is valid only when the scattered field,

$$u_s(\vec{r}) = u(\vec{r}) - u_0(\vec{r}), \quad (47)$$

is smaller than the incident field, u_0 . If the object is a homogeneous cylinder it is possible to express this condition as a function of the size of the object and the refractive index. Let the incident wave, $u_0(\vec{r})$, be an electromagnetic plane wave propagating in the direction of the unit vector, \vec{s} . For a large object, the field inside the object will not be well approximated by the incident field

$$u(\vec{r}) = u_{\text{object}}(\vec{r}) \neq A e^{jk_0 \vec{s} \cdot \vec{r}} \quad (48)$$

but instead will be a function of the change in refractive index, n_δ . Along a line through the center of the cylinder and parallel to the direction of propagation of the incident plane wave, the field inside the object becomes a slow (or fast) version of the incident wave, that is,

$$u_{\text{object}}(\vec{r}) = A e^{jk_0(1+n_\delta)\vec{s} \cdot \vec{r}}. \quad (49)$$

Since the wave is propagating through the object, the phase difference between the incident field and the field inside the object is approximately equal to the integral through the object of the change in refractive index. For a

homogeneous cylinder of radius a , the total phase shift through the object becomes

$$\text{Phase Change} = 4\pi n_\delta \frac{a}{\lambda} \quad (50)$$

where λ is the wavelength of the incident wave. For the Born approximation to be valid, a necessary condition is that the change in phase between the incident field and the wave propagating through the object be less than π . This condition can be expressed mathematically as

$$an_\delta < \frac{\lambda}{4}. \quad (51)$$

6.2.2 The First Rytov Approximation

Another approximation to the scattered field is the Rytov approximation which is valid under slightly different restrictions. It is derived by considering the total field to be represented as a complex phase or [Ish78]

$$u(\vec{r}) = e^{\phi(\vec{r})} \quad (52)$$

and rewriting the wave equation (17)

$$(\nabla^2 + k^2)u = 0 \quad (17)$$

as

$$\nabla^2 e^\phi + k^2 e^\phi = 0 \quad (53)$$

$$\nabla[\nabla\phi e^\phi] + k^2 e^\phi = 0 \quad (54)$$

$$\nabla^2 \phi e^\phi + (\nabla\phi)^2 e^\phi + k^2 e^\phi = 0 \quad (55)$$

and finally

$$(\nabla\phi)^2 + \nabla^2\phi + k_0^2 = -o(\vec{r}). \quad (56)$$

(Although all the fields, ϕ , are a function of \vec{r} , to simplify the notation the argument of these functions will be dropped.) Expressing the total complex phase, ϕ , as the sum of the incident phase function ϕ_0 and the scattered complex phase ϕ_s or

$$\phi(\vec{r}) = \phi_0(\vec{r}) + \phi_s(\vec{r}) \quad (57)$$

where

$$u_0(\vec{r}) = e^{\phi_0(\vec{r})}, \quad (58)$$

we find that

$$(\nabla\phi_0)^2 + 2\nabla\phi_0 \cdot \nabla\phi_s + (\nabla\phi_s)^2 + \nabla^2\phi_0 + \nabla^2\phi_s + k_0^2 + o(\vec{r}) = 0. \quad (59)$$

As in the Born approximation, it is possible to set the zero perturbation equation equal to zero. Doing this, we find that

$$k_0^2 + (\nabla\phi_0)^2 + \nabla^2\phi_0 = 0. \quad (60)$$

Substituting this into (59) we get

$$2\nabla\phi_0 \cdot \nabla\phi_s + \nabla^2\phi_s = -(\nabla\phi_s)^2 - o(\vec{r}). \quad (61)$$

This equation is still inhomogeneous but can be linearized by considering the relation

$$\nabla^2(u_0\phi_s) = \nabla(\nabla u_0 \cdot \phi_s + u_0\nabla\phi_s) \quad (62)$$

or by expanding the first derivative on the right-hand side of this equation

$$\nabla^2(u_0\phi_s) = \nabla^2u_0 \cdot \phi_s + 2\nabla u_0 \cdot \nabla\phi_s + u_0\nabla^2\phi_s. \quad (63)$$

Using a plane wave for the incident field,

$$u_0 = A e^{jk_0\vec{s} \cdot \vec{r}}, \quad (64)$$

we find

$$\nabla^2u_0 = -k_0^2u_0 \quad (65)$$

so that (63) may be rewritten as

$$2u_0\nabla\phi_0 \cdot \nabla\phi_s + u_0\nabla^2\phi_s = \nabla^2(u_0\phi_s) + k_0^2u_0\phi_s. \quad (66)$$

This result can be substituted into (61) to find

$$(\nabla^2 + k_0^2)u_0\phi_s = -u_0[(\nabla\phi_s)^2 + o(\vec{r})]. \quad (67)$$

The solution to this differential equation can again be expressed as an integral equation. This becomes

$$u_0\phi_s = \int_{V'} g(\vec{r} - \vec{r}') u_0[(\nabla\phi_s)^2 + o(\vec{r}')] d\vec{r}'. \quad (68)$$

Using the Rytov approximation we assume that the term in brackets in the above equation can be approximated by

$$(\nabla\phi_s)^2 + o(\vec{r}) = o(\vec{r}). \quad (69)$$

When this is done, the first-order Rytov approximation to the function $u_0\phi_s$ becomes

$$u_0\phi_s = \int_{V'} g(\vec{r} - \vec{r}') u_0(\vec{r}') o(\vec{r}') d\vec{r}'. \quad (70)$$

Thus ϕ_s , the complex phase of the scattered field, is given by

$$\phi_s(\vec{r}) = \frac{1}{u_0(\vec{r})} \int_{V'} g(\vec{r} - \vec{r}') u_0(\vec{r}') o(\vec{r}') d\vec{r}'. \quad (71)$$

Substituting the expression for u_B given in (40), we find that

$$\phi_s(\vec{r}) = \frac{u_B(\vec{r})}{u_0(\vec{r})}. \quad (72)$$

The Rytov approximation is valid under a less restrictive set of conditions than the Born approximation [Che60], [Kel69]. In deriving the Rytov approximation we made the assumption that

$$(\nabla \phi_s)^2 + o(\vec{r}) \approx o(\vec{r}). \quad (73)$$

Clearly this is true only when

$$o(\vec{r}) \gg (\nabla \phi_s)^2. \quad (74)$$

If $o(\vec{r})$ is written in terms of the change in refractive index

$$o(\vec{r}) = k_0^2 [n^2(\vec{r}) - 1] = k_0^2 [(1 + n_\delta(\vec{r}))^2 - 1] \quad (29)$$

and the square of the refractive index is expanded to find

$$o(\vec{r}) = k_0^2 [(1 + 2n_\delta(\vec{r}) + n_\delta^2(\vec{r})) - 1] \quad (75)$$

$$o(\vec{r}) = k_0^2 [2n_\delta(\vec{r}) + n_\delta^2(\vec{r})]. \quad (76)$$

To a first approximation, the object function is linearly related to the refractive index or

$$o(\vec{r}) \approx 2k_0^2 n_\delta(\vec{r}). \quad (77)$$

The condition needed for the Rytov approximation (see (74)) can be rewritten as

$$n_\delta \gg \frac{(\nabla \phi_s)^2}{k_0^2}. \quad (78)$$

This can be justified by observing that to a first approximation the scattered phase, ϕ_s , is linearly dependent on the refractive index change, n_δ , and therefore the first term in (73) can be safely ignored for small n_δ .

Unlike the Born approximation, the size of the object is not a factor in the Rytov approximation. The term $\nabla \phi_s$ is the change in the complex scattered phase per unit distance and by dividing by the wavenumber

$$k_0 = \frac{2\pi}{\lambda} \quad (79)$$

we find a necessary condition for the validity of the Rytov approximation is

$$n_\delta \gg \left[\frac{\nabla \phi_s \lambda}{2\pi} \right]^2. \quad (80)$$

Unlike the Born approximation, it is the change in scattered phase, ϕ_s , over one wavelength that is important and not the total phase. Thus, because of the ∇ operator, the Rytov approximation is valid when the phase change over a single wavelength is small.

Since the imaging process is carried out in terms of the field, u_B , defined in the previous subsection, we need to show a Rytov approximation expression for u_B . Estimating $u_B(\vec{r})$ for the Rytov case is slightly more difficult. In an experiment the total field, $u(\vec{r})$, is measured. An expression for $u_B(\vec{r})$ is found by recalling the expression for the Rytov solution to the total wave

$$u(\vec{r}) = u_0 + u_s(\vec{r}) = e^{\phi_0 + \phi_s} \quad (81)$$

and then rearranging the exponentials to find

$$u_s = e^{\phi_0 + \phi_s} - e^{\phi_0} \quad (82)$$

$$u_s = e^{\phi_0}(e^{\phi_s} - 1) \quad (83)$$

$$u_s = u_0(e^{\phi_s} - 1). \quad (84)$$

Inverting this to find an estimate for the scattered phase, ϕ_s , we obtain

$$\phi_s(\vec{r}) = \ln \left[\frac{u_s}{u_0} + 1 \right]. \quad (85)$$

Expanding ϕ_s in terms of (72) we obtain the following estimate for the Rytov estimate of $u_B(\vec{r})$:

$$u_B(\vec{r}) = u_0(\vec{r}) \ln \left[\frac{u_s}{u_0} + 1 \right]. \quad (86)$$

Since the natural logarithm is a multiple-valued function, one must be careful at each position to choose the correct value. For continuous functions this isn't difficult because only one value will satisfy the continuity requirement. On the other hand, for discrete (or sampled) signals the choice isn't nearly as simple and one must resort to a phase unwrapping algorithm to choose the proper phase. (Phase unwrapping has been described in a number of works [Tri77], [OCO78], [Kav84], [McG82].) Due to the “+1” factor inside the logarithmic term, this is only a problem if u_s is on the order of or larger than u_0 . Thus both the Born and the Rytov techniques can be used to estimate $u_B(\vec{r})$.

While the Rytov approximation is valid over a larger class of objects, it is possible to show that the Born and the Rytov approximations produce the

same result for objects that are small and deviate only slightly from the average refractive index of the medium. Consider first the Rytov approximation to the scattered wave. This is given by

$$u(\vec{r}) = e^{\phi_0 + \phi_s}. \quad (87)$$

Substituting an expression for the scattered phase, (72), and the incident field, (64), we find

$$u(\vec{r}) = e^{jk_0 \vec{s} \cdot \vec{r} + \exp(-jk_0 \vec{s} \cdot \vec{r}) u_B(\vec{r})} \quad (88)$$

or

$$u(\vec{r}) = u_0(\vec{r}) e^{\exp(-jk_0 \vec{s} \cdot \vec{r}) u_B(\vec{r})}. \quad (89)$$

For small u_B , the first exponential can be expanded in terms of its power series. Throwing out all but the first two terms we find that

$$u(\vec{r}) = u_0(\vec{r}) [1 + e^{-jk_0 \vec{s} \cdot \vec{r}} u_B(\vec{r})] \quad (90)$$

or

$$u(\vec{r}) = u_0(\vec{r}) + u_B(\vec{r}). \quad (91)$$

Thus for very small objects and perturbations the Rytov solution is approximately equal to the Born solution given in (40).

The similarity between the expressions for the first-order Born and Rytov solutions will form the basis of our reconstructions. In the Born approximation we measure the complex amplitude of the scattered field and use this as an estimate of the function u_B , while in the Rytov case we estimate u_B from the phase of the scattered field. Since the Rytov approximation is considered more accurate than the Born approximation it should provide a better estimate of u_B . In Section 6.5, after we have derived reconstruction algorithms based on the Fourier Diffraction Theorem, we will discuss simulations comparing the Born and the Rytov approximations.

6.3 The Fourier Diffraction Theorem

Fundamental to diffraction tomography is the *Fourier Diffraction Theorem*, which relates the Fourier transform of the measured forward scattered data with the Fourier transform of the object. *The theorem is valid when the inhomogeneities in the object are only weakly scattering.* The statement of the theorem is as follows:

When an object, $o(x, y)$, is illuminated with a plane wave as shown in Fig. 6.2, the Fourier transform of the forward scattered field measured on line TT' gives the values of the 2-D transform, $O(\omega_1, \omega_2)$, of the object along a semicircular arc in the frequency domain, as shown in the right half of the figure.

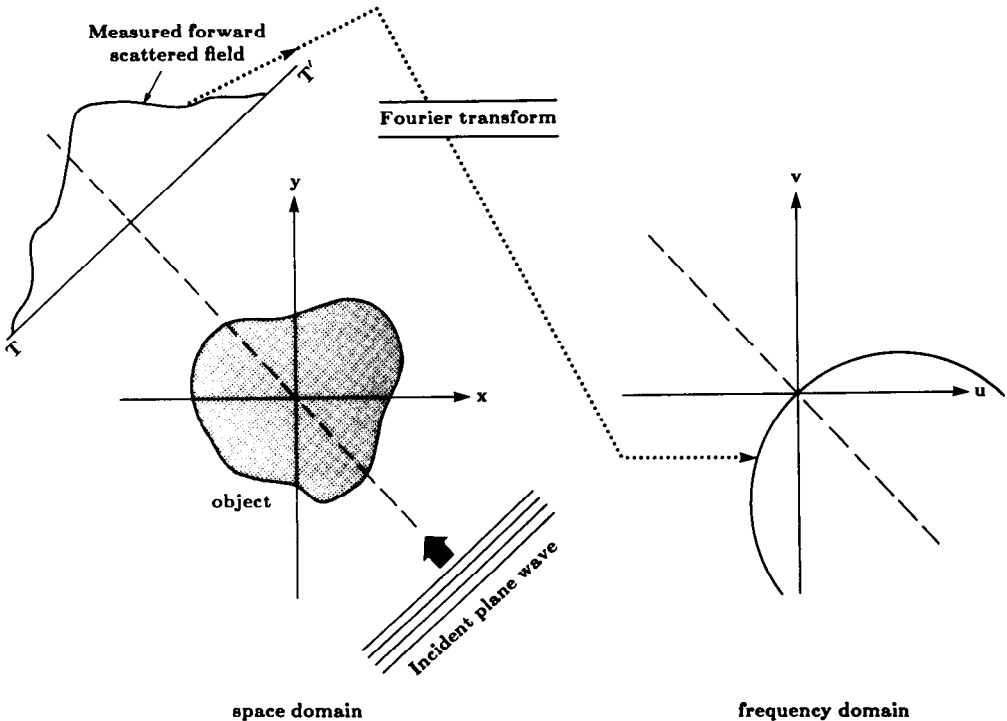


Fig. 6.2: *The Fourier Diffraction Theorem relates the Fourier transform of a diffracted projection to the Fourier transform of the object along a semicircular arc.* (From [Sla83].)

The importance of the theorem is made obvious by noting that if an object is illuminated by plane waves from many directions over 360° , the resulting circular arcs in the (ω_1, ω_2) -plane will fill up the frequency domain. The function $o(x, y)$ may then be recovered by Fourier inversion.

Before giving a short proof of the theorem, we would like to say a few words about the dimensionality of the object vis-à-vis that of the wave fields. Although the theorem talks about a two-dimensional object, what is actually meant is an object that doesn't vary in the z direction. In other words, the theorem is about any cylindrical object whose cross-sectional distribution is given by the function $o(x, y)$. The forward scattered fields are measured on a line of detectors along TT' in Fig. 6.2. If a truly three-dimensional object were illuminated by the plane wave, the forward scattered fields would now have to be measured by a planar array of detectors. The Fourier transform of the fields measured by such an array would give the values of the 3-D transform of the object over a spherical surface. This was first shown by Wolf [Wol69]. More recent expositions are given in [Nah82] and [Dev84], where the authors have also presented a new synthetic aperture procedure for a full three-dimensional reconstruction using only two rotational positions of the object. In this chapter, however, we will continue to work with two-dimensional objects in the sense described here. A recent work describing some of the errors in this approach is [LuZ84].

Earlier in this chapter, we expressed the scattered field due to a weakly scattering object as the convolution

$$u_B(\vec{r}) = \int o(\vec{r}') u_0(\vec{r}') g(\vec{r} - \vec{r}') d\vec{r}' \quad (92)$$

where $u_B(\vec{r})$ represents the complex amplitude of the field as in the Born approximation, or the incident field, $u_0(\vec{r})$, times the complex scattered phase, $\phi_s(\vec{r})$, as in the Rytov approximation. Starting from this integral there are two approaches to the derivation of the Fourier Diffraction Theorem. Many researchers [Mue79], [Gre78], [Dev82] have expanded the Green's function into its plane wave decomposition and then noted the similarity of the resulting expression and the Fourier transform of the object. The alternative approach consists of taking the Fourier transform of both sides of (92). In this work we will present both approaches to the derivation of the Fourier Diffraction Theorem; the first because the math is more straightforward, the second because it provides a greater insight into the difference between transmission and reflection tomography.

6.3.1 Decomposing the Green's Function

We will first consider the decomposition of the Green's function into its plane wave components.

The integral equation for the scattered field (92) can be considered as a convolution of the Green's function, $g(\vec{r} - \vec{r}')$, and the product of the object function, $o(\vec{r}')$, and the incident field, $u_0(\vec{r}')$. Consider the effect of a single plane wave illuminating an object. The forward scattered field will be measured at the receiver line as is shown in Fig. 6.3.

A single plane wave in two dimensions can be represented as

$$u_0(\vec{r}) = e^{j\vec{K} \cdot \vec{r}} \quad (93)$$

where $\vec{K} = (k_x, k_y)$ satisfies the relationship

$$k_0^2 = k_x^2 + k_y^2. \quad (94)$$

From earlier in this chapter, the two-dimensional Green's function is given by

$$g(\vec{r} | \vec{r}') = \frac{j}{4} H_0(k_0 |\vec{r} - \vec{r}'|) \quad (95)$$

and H_0 is the zero-order Hankel function of the first kind. The function H_0 has the plane wave decomposition [Mor53]

$$H_0(k |\vec{r} - \vec{r}'|) = \frac{1}{\pi} \int_{-\infty}^{\infty} \frac{1}{\beta} e^{j[\alpha(x-x') + \beta(y-y')]} d\alpha \quad (96)$$

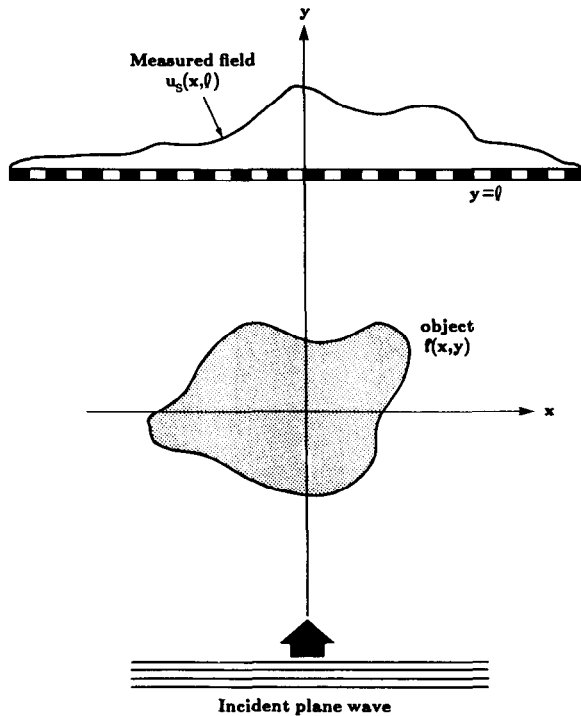


Fig. 6.3: A typical diffraction tomography experiment is shown. Here a single plane wave is used to illuminate the object and the scattered field is measured on the far side of the object. This is transmission tomography. (From [Pan83].)

where $\vec{r} = (x, y)$, $\vec{r}' = (x', y')$ and

$$\beta = \sqrt{k_0^2 - \alpha^2}. \quad (97)$$

Basically, (96) expresses a cylindrical wave, H_0 , as a superposition of plane waves. At all points, the wave centered at \vec{r}' is traveling outward; for points such that $y > y'$ the plane waves propagate upward while for $y < y'$ the plane waves propagate downward. In addition, for $|\alpha| \leq k_0$, the plane waves are of the ordinary type, propagating along the direction given by $\tan^{-1}(\beta/\alpha)$. However, for $|\alpha| > k_0$, β becomes imaginary, the waves decay exponentially and they are called *evanescent waves*. Evanescent waves are usually of no significance beyond about 10 wavelengths from the source.

Substituting this expression, (96), into the expression for the scattered field, (92), the scattered field can now be written

$$u_B(\vec{r}) = \frac{j}{4\pi} \int o(\vec{r}') u_0(\vec{r}') \int_{-\infty}^{\infty} \frac{1}{\beta} e^{j[\alpha(x-x') + \beta|y-y'|]} d\alpha d\vec{r}'. \quad (98)$$

In order to show the first steps in the proof of this theorem, we will now assume for notational convenience that the direction of the incident plane

wave is along the positive y -axis. Thus the incident field will be given by

$$u_0(\vec{r}) = e^{j\vec{s}_0 \cdot \vec{r}} \quad (99)$$

where $\vec{s}_0 = (0, k_0)$. Since in transmission imaging the scattered fields are measured by a linear array located at $y = l_0$, where l_0 is greater than any y -coordinate within the object (see Fig. 6.3), the term $|y - y'|$ in the above expression may simply be replaced by $l_0 - y'$ and the resulting form may be rewritten

$$u_B(x, y = l_0) = \frac{j}{4\pi} \int_{-\infty}^{\infty} d\alpha \int \frac{o(\vec{r}')}{\beta} e^{j[\alpha(x-x') + \beta(l_0-y')]} e^{jk_0 y'} d\vec{r}''. \quad (100)$$

Recognizing part of the inner integral as the two-dimensional Fourier transform of the object function evaluated at a frequency of $(\alpha, \beta - k_0)$ we find

$$u_B(x, y = l_0) = \frac{j}{4\pi} \int_{-\infty}^{\infty} \frac{1}{\beta} e^{j(\alpha x + \beta l_0)} O(\alpha, \beta - k_0) d\alpha \quad (101)$$

where O has been used to designate the two-dimensional Fourier transform of the object function.

Let $U_B(\omega, l_0)$ denote the Fourier transform of the one-dimensional scattered field, $u_B(x, l_0)$, with respect to x , that is,

$$U_B(\omega, l_0) = \int_{-\infty}^{\infty} u_B(x, l_0) e^{-j\omega x} dx. \quad (102)$$

As mentioned before, the physics of wave propagation dictate that the highest angular spatial frequency in the measured scattered field on the line $y = l_0$ is unlikely to exceed k_0 . Therefore, in almost all practical situations, $U_s(\omega, l_0) = 0$ for $|\omega| > k_0$. This is consistent with neglecting the evanescent modes as described earlier.

If we take the Fourier transform of the scattered field by substituting (101) into (102) and using the following property of Fourier integrals

$$\int_{-\infty}^{\infty} e^{j(\omega - \alpha)x} dx = 2\pi\delta(\omega - \alpha) \quad (103)$$

where $\delta(\cdot)$ is the Dirac delta function we discussed in Chapter 2, we find

$$U_B(\alpha, l_0) = \frac{j}{2\sqrt{k_0^2 - \alpha^2} l_0} e^{j\sqrt{k_0^2 - \alpha^2} l_0} O(\alpha, \sqrt{k_0^2 - \alpha^2} - k_0) \quad \text{for } |\alpha| < k_0. \quad (104)$$

This expression relates the two-dimensional Fourier transform of the object to

the one-dimensional Fourier transform of the field at the receiver line. The factor

$$\frac{j}{2\sqrt{k_0^2 - \alpha^2}} e^{j\sqrt{k_0^2 - \alpha^2}l_0} \quad (105)$$

is a simple constant for a fixed receiver line. As α varies from $-k_0$ to k_0 , the coordinates $(\alpha, \sqrt{k_0^2 - \alpha^2} - k_0)$ in the Fourier transform of the object function trace out a semicircular arc in the (u, v) -plane as shown in Fig. 6.2. This proves the theorem.

To summarize, if we take the Fourier transform of the forward scattered data when the incident illumination is propagating along the positive y -axis, the resulting transform will be zero for angular spatial frequencies $|\alpha| > k_0$. For $|\alpha| < k_0$, the transform of the data gives values of the Fourier transform of the object on the semicircular arc shown in Fig. 6.2 in the (u, v) -plane. The endpoints of the semicircular arc are at a distance of $\sqrt{2}k_0$ from the origin in the frequency domain.

6.3.2 Fourier Transform Approach

Another approach to the derivation of the Fourier Diffraction Theorem is possible if the scattered field

$$u_B(\vec{r}) = \int o(\vec{r}') u_0(\vec{r}') g(\vec{r} - \vec{r}') d\vec{r}' \quad (106)$$

is considered entirely in the Fourier domain. The plots of Fig. 6.4 will be used to illustrate the various transformations that take place. Again, consider the effect of a single plane wave illuminating an object. The forward scattered field will be measured at the receiver line as is shown in Fig. 6.3.

The integral equation for the scattered field, (106), can be considered as a convolution of the Green's function, $g(\vec{r} - \vec{r}')$, and the product of the object function, $o(\vec{r}')$, and the incident field, $u_0(\vec{r}')$. First define the following Fourier transform pairs:

$$\begin{aligned} o(\vec{r}) &\leftrightarrow O(\vec{K}) \\ g(\vec{r} - \vec{r}') &\leftrightarrow G(\vec{K}) \\ u(\vec{r}) &\leftrightarrow U(\vec{K}). \end{aligned} \quad (107)$$

The integral solution to the wave equation, (40), can now be written in terms of these Fourier transforms, that is,

$$U_s(\vec{\Lambda}) = G(\vec{\Lambda}) \{ O(\vec{\Lambda}) * U_0(\vec{\Lambda}) \} \quad (108)$$

where $*$ has been used to represent convolution and $\vec{\Lambda} = (\alpha, \gamma)$. In (93) an expression for u_0 was presented. Its Fourier transform is given by

$$U_0(\vec{\Lambda}) = 2\pi\delta(\vec{\Lambda} - \vec{K}) \quad (109)$$

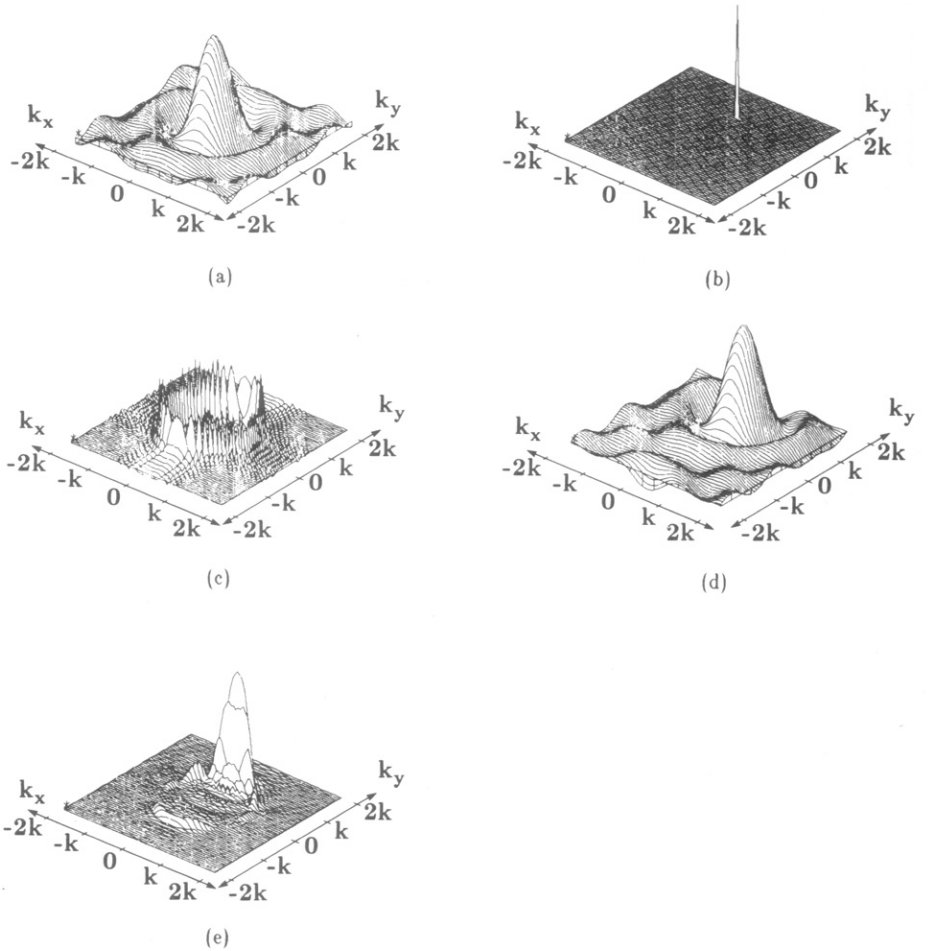


Fig. 6.4: Two-dimensional Fourier representation of the Helmholtz equation. (a) is the Fourier transform of the object, in this case a cylinder, (b) is the Fourier transform of the incident field, (c) is the Fourier transform of the Green's function in (95), (d) shows the frequency domain convolution of (a) and (b), and finally (e) is the product in the frequency domain of (c) and (d). (From [Sla83].)

and thus the convolution of (108) becomes a shift in the frequency domain or

$$O(\vec{\Lambda}) * U_0(\vec{\Lambda}) = 2\pi O(\vec{\Lambda} - \vec{K}). \quad (110)$$

This convolution is illustrated in Figs. 6.4(a)-(c) for a plane wave propagating with direction vector, $\vec{K} = (0, k_0)$. Fig. 6.4(a) shows the Fourier transform of a single cylinder of radius 1λ and Fig. 6.4(b) shows the Fourier transform of the incident field. The resulting multiplication in the space domain or convolution in the frequency domain is shown in Fig. 6.4(c).

To find the Fourier transform of the Green's function the Fourier transform of (32) is calculated to find

$$(-\Lambda^2 + k_0^2)G(\vec{\Lambda} | \vec{r}') = -e^{-j\vec{\Lambda} \cdot \vec{r}'}. \quad (111)$$

Rearranging terms we see that

$$G(\vec{\Lambda} \mid \vec{r}') = \frac{e^{-j\vec{\Lambda} \cdot \vec{r}'}}{\Lambda^2 - k_0^2} \quad (112)$$

which has a singularity for all $\vec{\Lambda}$ such that

$$|\Lambda|^2 = \alpha^2 + \gamma^2 = k_0^2. \quad (113)$$

An approximation to $G(\vec{\Lambda})$ is shown in Fig. 6.4(d).

The Fourier transform representation in (112) can be misleading because it represents a point scatterer as both a sink and a source of waves. A single plane wave propagating from left to right can be considered in two different ways depending on your point of view. From the left side of the scatterer, the point scatterer represents a sink to the wave, while to the right of the scatterer the wave is spreading from a source point. Clearly, it's not possible for a scatterer to be both a point source and a sink. Later, when our expression for the scattered field is inverted, it will be necessary to choose a solution that leads to outgoing waves only.

The effect of the convolution shown in (106) is a multiplication in the frequency domain of the shifted object function, (110), and the Green's function, (112), evaluated at $\vec{r}' = 0$. The scattered field is written as

$$U_s(\vec{\Lambda}) = 2\pi \frac{O(\vec{\Lambda} - \vec{K})}{\Lambda^2 - k^2}. \quad (114)$$

This result is shown in Fig. 6.4(e) for a plane wave propagating along the y -axis. Since the largest frequency domain components of the Green's function satisfy (113), the Fourier transform of the scattered field is dominated by a shifted and sampled version of the object's Fourier transform.

We will now derive an expression for the field at the receiver line. For simplicity we will continue to assume that the incident field is propagating along the positive y -axis or $\vec{K} = (0, k_0)$. The scattered field along the receiver line ($x, y = l_0$) is simply the inverse Fourier transform of the field in (114). This is written as

$$u(x, y = l_0) = \frac{1}{4\pi^2} \int_{-\infty}^{\infty} \int_{-\infty}^{\infty} U_s(\vec{\Lambda}) e^{j\vec{\Lambda} \cdot \vec{r}} d\alpha d\gamma \quad (115)$$

which, using (114), can be expressed as

$$u_s(x, y = l_0) = \frac{1}{4\pi^2} \int_{-\infty}^{\infty} \int_{-\infty}^{\infty} \frac{O(\alpha, \gamma - k_0)}{\alpha^2 + \gamma^2 - k_0^2} e^{j(\alpha x + \gamma l_0)} d\alpha d\gamma. \quad (116)$$

We will first find the integral with respect to γ . For a given α , the integral has a singularity for

$$\gamma_{1,2} = \pm \sqrt{k_0^2 - \alpha^2}. \quad (117)$$

Using contour integration we can evaluate the integral with respect to γ along the path shown in Fig. 6.5. By adding $1/2\pi$ of the residue at each pole we find

$$u_s(x, y) = \frac{1}{2\pi} \int \Gamma_1(\alpha; y) e^{j\alpha x} d\alpha + \frac{1}{2\pi} \int \Gamma_2(\alpha; y) e^{j\alpha x} d\alpha \quad (118)$$

where

$$\Gamma_1 = \frac{jO(\alpha, \sqrt{k_0^2 - \alpha^2} - k_0)}{2\sqrt{k_0^2 - \alpha^2}} e^{j\sqrt{k_0^2 - \alpha^2} l_0} \quad (119)$$

$$\Gamma_2 = \frac{-jO(\alpha, \sqrt{k_0^2 - \alpha^2} - k_0)}{2\sqrt{k_0^2 - \alpha^2}} e^{-j\sqrt{k_0^2 - \alpha^2} l_0}. \quad (120)$$

Examining the above pair of equations we see that Γ_1 represents the solution in terms of plane waves traveling along the positive y -axis, while Γ_2 represents plane waves traveling in the $-y$ direction.

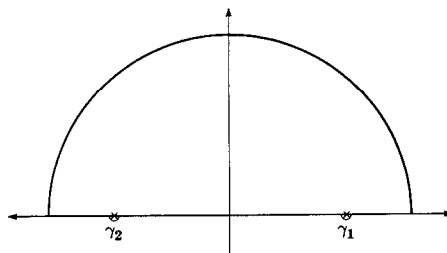
As was discussed earlier, the Fourier transform of the Green's function (112) represents the field due to both a point source and a point sink, but the two solutions are distinct for receiver lines that are outside the extent of the object. First consider the scattered field along the line $y = l_0$ where l_0 is greater than the y -coordinate of all points in the object. Since all scattered fields originate in the object, plane waves propagating along the positive y -axis represent outgoing waves while waves propagating along the negative y -axis represent waves due to a point sink. Thus for $y >$ object (i.e., the receiver line is above the object) the outgoing scattered waves are represented by Γ_1 or

$$u_s(x, y) = \frac{1}{2\pi} \int \Gamma_1(\alpha; y) e^{j\alpha x} d\alpha, \quad y > \text{object}. \quad (121)$$

Fig. 6.5: Integration path in the complex plane for inverting the two-dimensional Fourier transform of the scattered field. The correct pole must be chosen to lead to outgoing fields. (From [Sla84].)

Conversely, for a receiver along a line $y = l_0$ where l_0 is less than the y -coordinate of any point in the object, the scattered field is represented by Γ_2 or

$$u_s(x, y) = \frac{1}{2\pi} \int \Gamma_2(\alpha; y) e^{j\alpha x} d\alpha, \quad y < \text{object}. \quad (122)$$



In general, the scattered field will be written as

$$u_s(x, y) = \frac{1}{2\pi} \int \Gamma(\alpha; y) e^{j\alpha x} d\alpha \quad (123)$$

and it will be understood that values that lead only to outgoing waves should be chosen for the square root in the expression for Γ .

Taking the Fourier transform of both sides of (123) we find that

$$\int u(x, y = l_0) e^{-j\alpha x} dx = \Gamma(\alpha, l_0). \quad (124)$$

But since by (119) and (120), $\Gamma(\alpha, l_0)$ is equal to a phase shifted version of the object function, the Fourier transform of the scattered field along the line $y = l_0$ is related to the Fourier transform of the object along a circular arc. The use of the contour integration is further justified by noting that only those waves that satisfy the relationship

$$\alpha^2 + \gamma^2 = k_0^2 \quad (125)$$

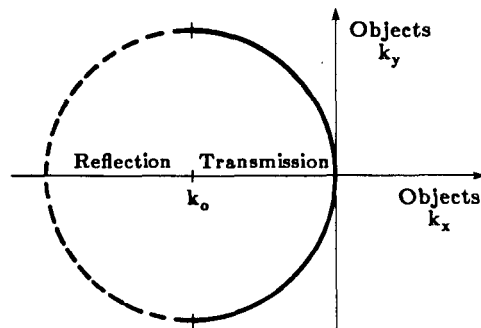
will be propagated and thus it is safe to ignore all waves not on the k_0 -circle.

This result is diagrammed in Fig. 6.6. The circular arc represents the locus of all points (α, γ) such that $\gamma = \sqrt{k_0^2 - \alpha^2}$. The solid line shows the outgoing waves for a receiver line at $y = l_0$ above the object. This can be considered transmission tomography. Conversely, the broken line indicates the locus of solutions for the reflection tomography case, or $y = l_0$ is below the object.

6.3.3 Short Wavelength Limit of the Fourier Diffraction Theorem

Fig. 6.6: Estimates of the two-dimensional Fourier transform of the object are available along the solid arc for transmission tomography and the broken arc for reflection tomography. (Adapted from [Sla84].)

While at first the derivations of the Fourier Slice Theorem and the Fourier Diffraction Theorem seem quite different, it is interesting to note that in the limit of very high energy waves or, equivalently, very short wavelengths the Fourier Diffraction Theorem approaches the Fourier Slice Theorem. Recall that the Fourier transform of a diffracted projection corresponds to samples of the two-dimensional Fourier transform of an object along a semicircular arc.



The radius of the arc shown in Fig. 6.2 is equal to k_0 which is given by

$$k_0 = \frac{2\pi}{\lambda} \quad (126)$$

and λ is the wavelength of the energy. As the wavelength is decreased, the wavenumber, k_0 , and the radius of the arc in the object's Fourier domain grow. This process is illustrated in Fig. 6.7 where we have shown the semicircular arcs resulting from diffraction experiments at seven different frequencies.

An example might make this idea clearer. An ultrasonic tomography experiment might be carried out at a frequency of 5 MHz which corresponds to a wavelength in water of 0.3 mm. This corresponds to a k_0 of 333 radians/meter. On the other hand, a hypothetical coherent x-ray source with a 100-keV beam has a wavelength of 0.012 μm . The result is that a diffraction experiment with x-rays can give samples along an arc of radius 5×10^8 radians/meter. Certainly for all physiological features (i.e., resolutions of < 1000 radians/meter) the arc could be considered to be a straight line and the Fourier Slice Theorem an excellent model for relating the transforms of the projections with the transform of the object.

6.3.4 The Data Collection Process

The best that can be hoped for in any tomographic experiment is to estimate the Fourier transform of the object for all frequencies within a disk centered at the origin. For objects whose spectra have no frequency content outside the disk, the reconstruction procedure is perfect.

There are several different procedures that can be used to estimate the object function from the scattered field. A single plane wave provides exact information (up to a frequency of $\sqrt{2}k_0$) about the Fourier transform of the object along a semicircular arc. Two of the simplest procedures involve

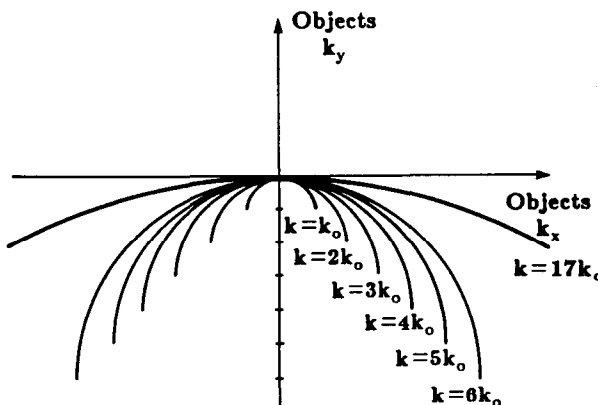


Fig. 6.7: As the frequency of the experiment goes up (wavelength goes down) the radius of the arc increases until the scattered field is closely approximated by the Fourier Slice Theorem discussed in Chapter 3.

changing the orientation and frequency of the incident plane waves to move the frequency domain arcs to a new position. By appropriately choosing an orientation and a frequency it is possible to estimate the Fourier transform of the object at any given frequency. In addition, it is possible to change the radius of the semicircular arc by varying the frequency of the incident field and thus generating an estimate of the entire Fourier transform of the object.

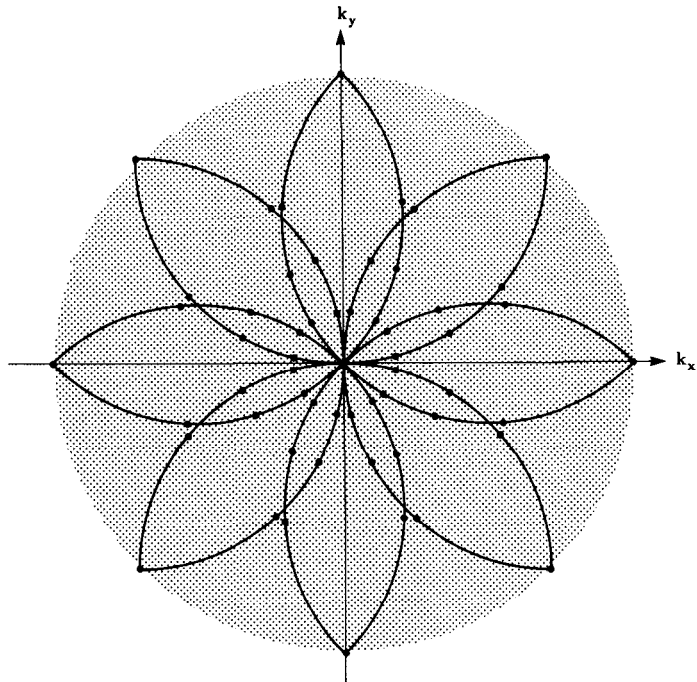
The most straightforward data collection procedure was discussed by Mueller *et al.* [Mue80] and consists of rotating the object and measuring the scattered field for different orientations. Each orientation will produce an estimate of the object's Fourier transform along a circular arc and these arcs will rotate as the object is rotated. When the object has rotated through a full 360° an estimate of the object will be available for the entire Fourier disk.

The coverage for this method is shown in Fig. 6.8 for a simple experiment with eight projections of nine samples each. Notice that there are two arcs that pass through each point of Fourier space. Generally, it will be necessary to choose one estimate as better.

On the other hand, if the reflected data are collected by measuring the field on the same side of the object as the source, then estimates of the object are available for frequencies greater than $\sqrt{2}k_0$. This follows from Fig. 6.6.

Nahamoo and Kak [Nah82], [Nah84] and Devaney [Dev84] have proposed a method that requires only two rotational views of an object. Consider an arbitrary source of waves in the transmitter plane as shown in Fig. 6.9. The

Fig. 6.8: With plane wave illumination, estimates of the object's two-dimensional Fourier transform are available along the circular arcs.



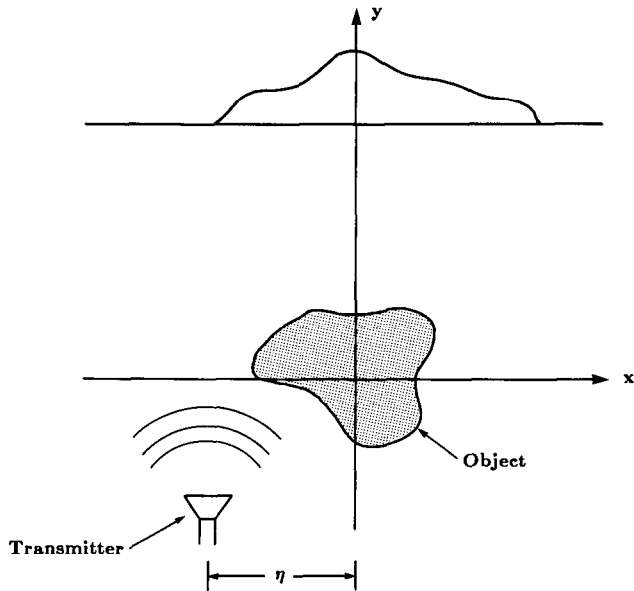


Fig. 6.9: A typical synthetic aperture tomography experiment is shown. A transmitter is scanned past the object. For each transmitter position the scattered field is measured. Later, appropriate phases are added to the projections to synthesize any incident plane wave. (From [Sla83].)

transmitted field, u_t , can be represented as a weighted set of plane waves by taking the Fourier transform of the transmitter aperture function [Goo68]. Doing this we find

$$u_t(x) = \frac{1}{4\pi^2} \int_{-\infty}^{\infty} A_t(k_x) e^{jk_x x} dk_x. \quad (127)$$

Moving the source to a new position, η , the plane wave decomposition of the transmitted field becomes

$$u_t(x; \eta) = \frac{1}{4\pi^2} \int_{-\infty}^{\infty} (A_t(k_x) e^{jk_x \eta}) e^{jk_x x} dk_x. \quad (128)$$

Given the plane wave decomposition, the incident field in the plane follows simply as

$$u_i(\eta; x, y) = \int_{-\infty}^{\infty} \left(\frac{1}{4\pi^2} A_t(k_x) e^{jk_x \eta} \right) e^{j(k_x x + k_y y)} dk_x. \quad (129)$$

In (124) we presented an equation for the scattered field from a single plane wave. Because of the linearity of the Fourier transform the effect of each plane wave, $e^{j(k_x x + k_y y)}$, can be weighted by the expression in brackets above and superimposed to find the Fourier transform of the total scattered field due to the incident field $u_i(x; \eta)$ as [Nah82]

$$U_s(\eta; \alpha) = \int_{-\infty}^{\infty} (A_t(k_x) e^{jk_x \eta}) \frac{O(\alpha - k_x, \gamma - k_y)}{j2\gamma} dk_x. \quad (130)$$

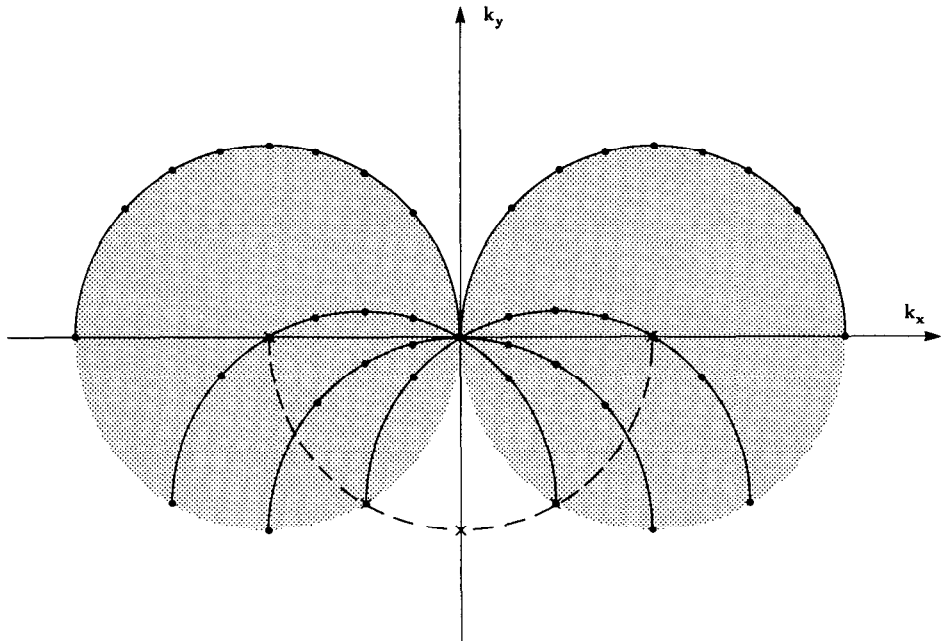
Taking the Fourier transform of both sides with respect to the transmitter position, η , we find that

$$U_s(k_x; \alpha) = A_t(k_x) \frac{O(\alpha - k_x, \gamma - k_y)}{j2\gamma}. \quad (131)$$

By collecting the scattered field along the receiver line as a function of transmitter position, η , we have an expression for the scattered field. Like the simpler case with plane wave incidence, the scattered field is related to the Fourier transform of the object along an arc. Unlike the previous case, though, the coverage due to a single view of the object is a pair of circular disks as shown in Fig. 6.10. Here a single view consists of transmitting from all positions in a line and measuring the scattered field at all positions along the receiver line. By rotating the object by 90° it is possible to generate the complementary disk and to fill the Fourier domain.

The coverage shown in Fig. 6.10 is constructed by calculating $(\bar{K} - \bar{\Lambda})$ for all vectors (\bar{K}) and $(\bar{\Lambda})$ that satisfy the experimental constraints. Not only must each vector satisfy the wave equation but it is also necessary that only forward traveling plane waves be used. The broken line in Fig. 6.10 shows the valid propagation vectors $(-\bar{\Lambda})$ for the transmitted waves. To each possible vector $(-\bar{\Lambda})$ a semicircular set of vectors representing each possible received wave can be added. The locus of received plane waves is shown as a solid semicircle centered at each of the transmitted waves indicated by an \times .

Fig. 6.10: Estimates of the Fourier transform of an object in the synthetic aperture experiment are available in the shaded region.



The entire coverage for the synthetic aperture approach is shown as the shaded areas.

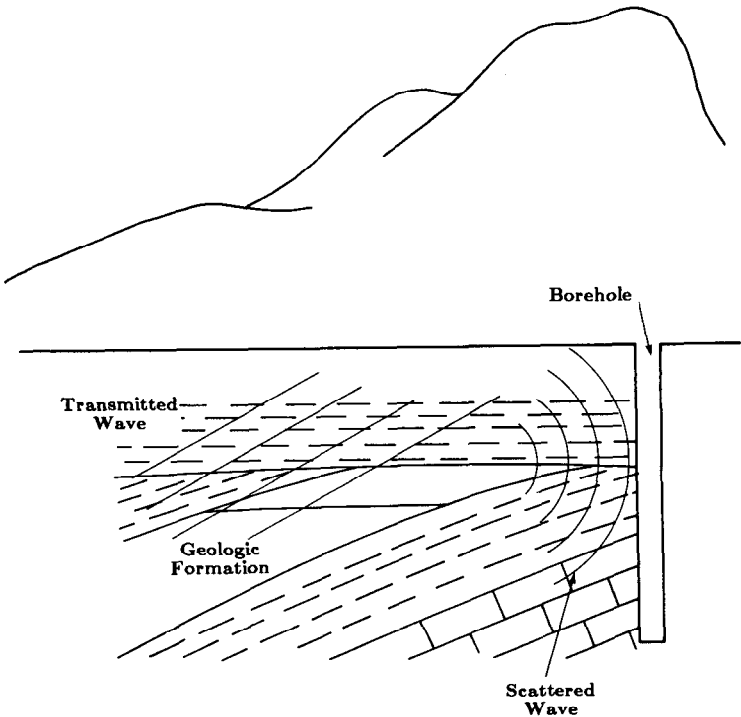
In geophysical imaging it is not possible to generate or receive waves from all positions around the object. If it is possible to drill a borehole, then it is possible to perform vertical seismic profiling (VSP) [Dev83] and obtain information about most of the object. A typical experiment is shown in Fig. 6.11. So as to not damage the borehole, acoustic waves are generated at the surface using acoustic detonators or other methods and the scattered field is measured in the borehole.

The coverage in the frequency domain is similar to the synthetic aperture approach in [Nah84]. Plane waves at an arbitrary downward direction are synthesized by appropriately phasing the transmitting transducers. The receivers will receive any waves traveling to the right. The resulting coverage for this method is shown in Fig. 6.12(a). If we further assume that the object function is real valued, we can use the symmetry of the Fourier transform for real-valued functions to obtain the coverage in Fig. 6.12(b).

It is also possible to perform such experiments with broadband illumination [Ken82]. So far we have only considered narrow band illumination wherein the field at each point can be completely described by its complex amplitude.

Now consider a transducer that illuminates an object with a plane wave of the form $A_r(t)$. It can still be called a plane wave because the amplitude of the

Fig. 6.11: A typical vertical seismic profiling (VSP) experiment.



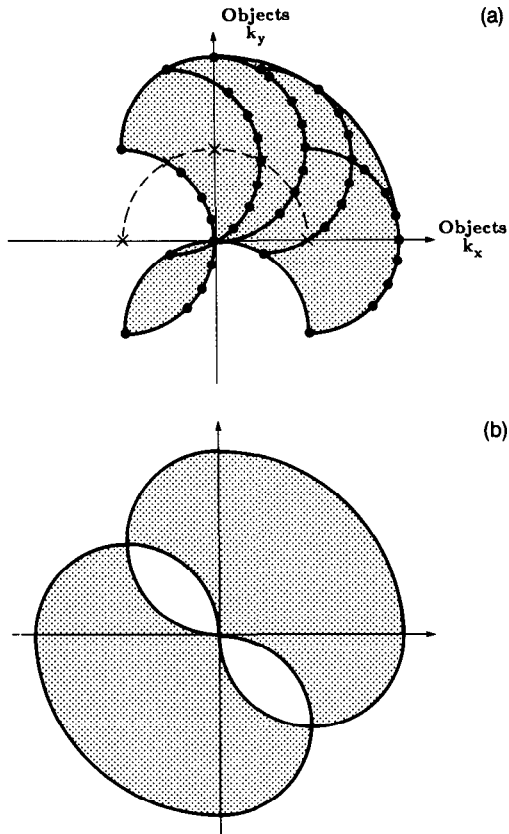


Fig. 6.12: Available estimate of the Fourier transform of an object for a VSP experiment (a). If the object function is real valued, then the symmetry of the Fourier transform can be used to estimate the object in the region shown in (b).

field along planes perpendicular to the direction of travel is constant. Taking the Fourier transform in the time domain we can decompose this field into a number of experiments, each at a different temporal frequency, ω . We let

$$A_t(x, y, \omega) = \int_{-\infty}^{\infty} A_t(x, y, t) e^{+j\omega t} dt \quad (132)$$

where the sign on the exponential is positive because of the convention defined in Section 6.1.1.

Given the amplitude of the field at each temporal frequency, it is straightforward to decompose the field into plane wave components by finding its Fourier transform along the transmitter plane. Each plane wave component is then described as a function of spatial frequency, $k_\omega = \sqrt{k_x^2 + k_y^2}$, and temporal frequency, ω . The temporal frequency ω is related to k_ω by

$$k_\omega = \frac{c}{\omega} \quad (133)$$

where c is the speed of propagation in the media and the wave vector (k_x, k_y) satisfies the wave equation

$$k_x^2 + k_y^2 = k_\omega^2. \quad (134)$$

If a unit amplitude plane wave illumination of spatial frequency k_x and a temporal frequency ω leads to a scattered plane wave with amplitude $u_s(k_x, \omega)$, then the total scattered field is given by a weighted superposition of the scattered fields or

$$u_s(x, y; t) = \frac{1}{2\pi} \int_{-\infty}^{\infty} d\omega \int_{-k_\omega}^{k_\omega} dk_x A_t(k_x, \omega) e^{-j\omega t} u_s(k_x, \omega; y) e^{j(k_x x + k_y y)}. \quad (135)$$

For plane wave incidence the coverage for this method is shown in Fig. 6.13(a). Fig. 6.13(b) shows that by doing four experiments at 0, 90, 180, and 270° it is possible to gather information about the entire object.

6.4 Interpolation and a Filtered Backpropagation Algorithm for Diffracting Sources

In our proof of the Fourier Diffraction Theorem, we showed that when an object is illuminated with a plane wave traveling in the positive y direction, the Fourier transform of the forward scattered fields gives values of the arc shown in Fig. 6.2. Therefore, if an object is illuminated from many different directions, we can, in principle, fill up a disk of diameter $\sqrt{2}k$ in the frequency domain with samples of $O(\omega_1, \omega_2)$, which is the Fourier transform of the object, and then reconstruct the object by direct Fourier inversion. Therefore, we can say that diffraction tomography determines the object up to a maximum angular spatial frequency of $\sqrt{2}k$. To this extent, the reconstructed object is a low pass version of the original. In practice, the loss of resolution caused by this bandlimiting is negligible, being more influenced by considerations such as the aperture sizes of the transmitting and receiving elements, etc.

The fact that the frequency domain samples are available over circular arcs, whereas for convenient display it is desirable to have samples over a rectangular lattice, is a source of computational difficulty in reconstruction algorithms for diffracting tomography. To help the reader visualize the distribution of the available frequency domain information, we have shown in Fig. 6.8 the sampling points on a circular arc grid, each arc in this grid corresponding to the transform of one projection. It should also be clear from this figure that by illuminating the object over 360° a *double* coverage of the frequency domain is generated; note, however, that this double coverage is uniform. We may get a complete coverage of the frequency domain with illumination restricted to a portion of 360°; however, in that case there would

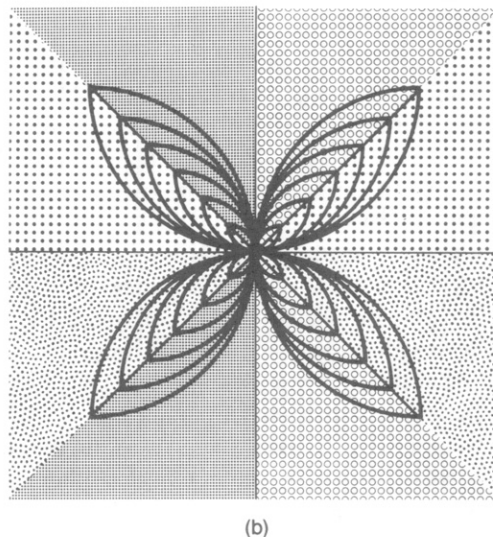
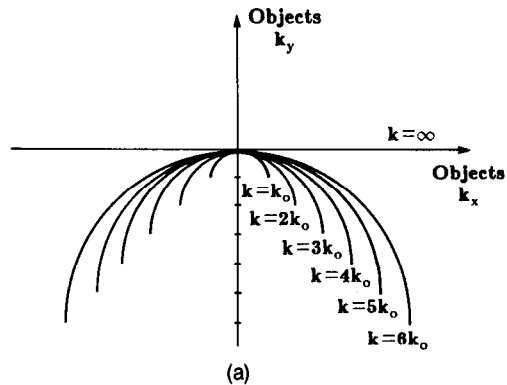


Fig. 6.13: (a) Estimates of the Fourier transform of an object for broadband illumination. With four views the coverage shown in (b) is possible.

be patches in the (ω_1, ω_2) -plane where we would have a double coverage. In reconstructing from circular arc grids to rectangular grids, it is often easier to contend with a uniform double coverage, as opposed to a coverage that is single in most areas and double in patches.

However, for some applications that do not lend themselves to data collection from all possible directions, it is useful to bear in mind that it is not necessary to go completely around an object to get complete coverage of the frequency domain. In principle, it should be possible to get an equal quality reconstruction when illumination angles are restricted to a 180° plus an interval, the angles in excess of 180° being required to complete the coverage of the frequency domain.

There are two computational strategies for reconstructing the object from the measurements of the scattered field. As pointed out in [Sou84a], the two

algorithms can be considered as interpolation in the frequency domain and interpolation in the space domain; and are analogous to the direct Fourier inversion and backprojection algorithms of conventional tomography. Unlike conventional tomography, where backprojection is the preferred approach, the computational expense of space domain interpolation of diffracted projections makes frequency domain interpolation the preferred approach for diffraction tomography reconstructions.

The remainder of this section will consist of derivations of the frequency domain and space domain interpolation algorithms. In both cases we will assume plane wave illumination; the reader is referred to [Dev82], [Pan83] for reconstruction algorithms for the synthetic aperture approach and to [Sou84b] for the general case.

6.4.1 Frequency Domain Interpolation

There are two schemes for frequency domain interpolation. The more conventional approach is polynomial based and assumes that the data near each grid point can be approximated by polynomials. This is the classical numerical analysis approach to the problem. A second approach is known as the unified frequency domain reconstruction (UFR) and interpolates data in the frequency domain by assuming that the space domain reconstruction should be spatially limited. We will first describe polynomial interpolation.

In order to discuss the frequency domain interpolation between a circular arc grid on which the data are generated by diffraction tomography and a rectangular grid suitable for image reconstruction, we must first select parameters for representing each grid and then write down the relationship between the two sets of parameters.

In (104), $U_B(\omega, l_0)$ was used to denote the Fourier transform of the transmitted data when an object is illuminated with a plane wave traveling along the positive y direction. We now use $U_{B,\phi}(\omega)$ to denote this Fourier transform, where the subscript ϕ indicates the angle of illumination. This angle is measured as shown in Fig. 6.14. Similarly, $Q(\omega, \phi)$ will be used to indicate the values of $O(\omega_1, \omega_2)$ along a semicircular arc oriented at an angle ϕ as shown in Fig. 6.15 or

$$Q(\omega, \sqrt{k_0^2 - \omega^2} - k_0), \quad |\omega| < k_0. \quad (136)$$

Therefore, when an illuminating plane wave is incident at angle ϕ , the equality in (104) can be rewritten as

$$U_{B,\phi}(\omega) = \frac{j}{2} \frac{1}{\sqrt{k^2 - \omega^2}} \exp[jl\sqrt{k^2 - \omega^2}] Q(\omega, \phi) \quad \text{for } |\omega| < k. \quad (137)$$

In most cases the transmitted data will be uniformly sampled in space, and a *discrete* Fourier transform of these data will generate uniformly spaced

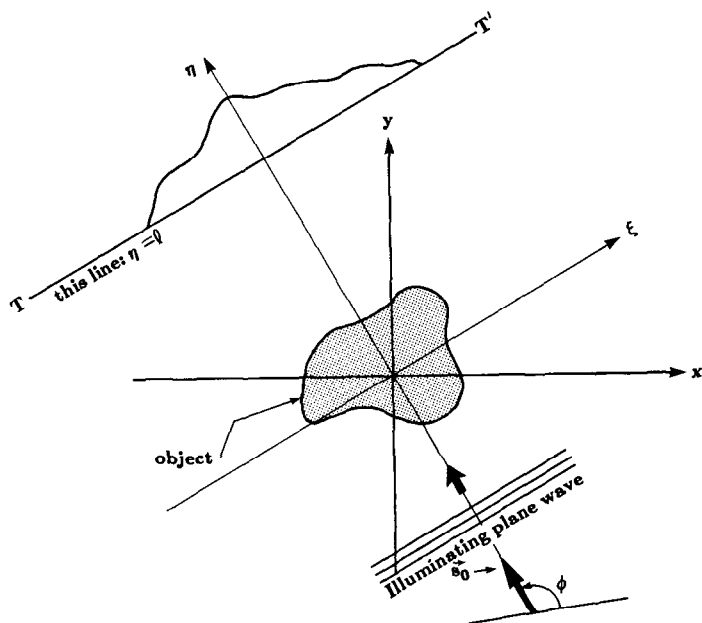
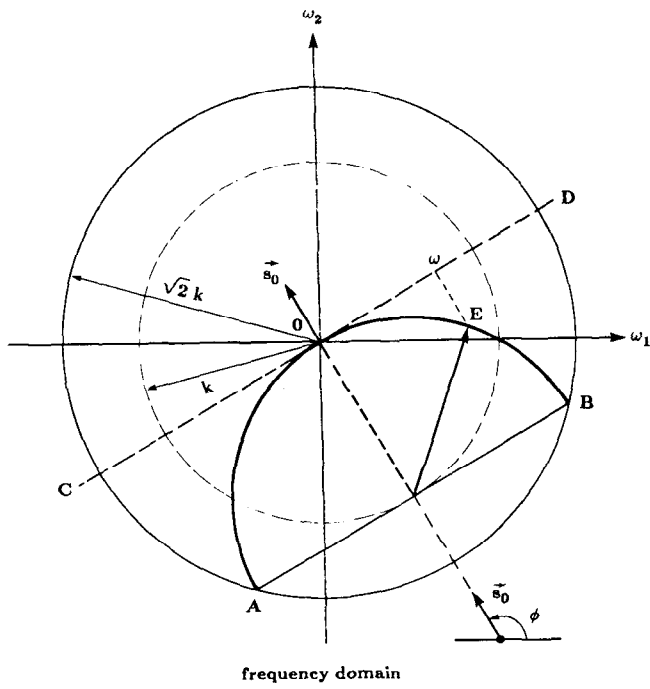


Fig. 6.14: The angle ϕ is used to identify each diffraction projection. (From [Pan83].)

Fig. 6.15: Each projection is measured using the $\phi - \omega$ coordinate system shown here. (From [Kak85].)



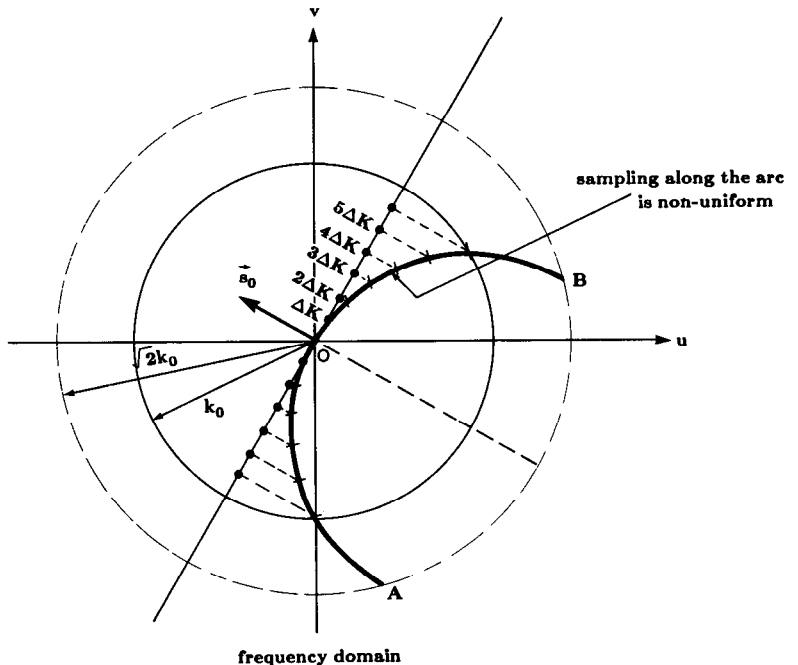
samples of $U_{B,\phi}(\omega)$ in the ω domain. Since $Q(\omega)$ is the Fourier transform of the object along the circular arc AOB in Fig. 6.15 and since κ is the projection of a point on the circular arc on the tangent line CD , the uniform samples of Q in κ translate into nonuniform samples along the arc AOB as shown in Fig. 6.16. We will therefore designate each point on the arc AOB by its (ω, ϕ) parameters. [Note that (ω, ϕ) are *not* the polar coordinates of a point on arc AOB in Fig. 6.15. Therefore, ω is *not* the radial distance in the (ω_1, ω_2) -plane. For point E shown, the parameter ω is obtained by projecting E onto line CD .] We continue to denote the rectangular coordinates in the frequency domain by (ω_1, ω_2) .

Before we present relationships between (ω, ϕ) and (ω_1, ω_2) , it must be mentioned that we must consider separately the points generated by the AO and OB portions of the arc AOB as ϕ is varied from 0 to 2π . We do this because, as mentioned before, the arc AOB generates a double coverage of the frequency domain, as ϕ is varied from 0 to 2π , which is undesirable for discussing a one-to-one transformation between the (ω, ϕ) parameters and the (ω_1, ω_2) coordinates.

We now reserve (ω, ϕ) parameters to denote the arc grid generated by the portion OB as shown in Fig. 6.15. It is important to note that for this arc grid, ω varies from 0 to k and ϕ from 0 to 2π .

We now present the transformation equations between (ω, ϕ) and (ω_1, ω_2) . We accomplish this in a slightly roundabout manner by first defining polar

Fig. 6.16: Uniformly sampling the projection in the space domain leads to uneven spacing of the samples of the Fourier transform of the object along the semicircular arc. (Adapted from [Pan83].)



coordinates (Ω, θ) in the (ω_1, ω_2) -plane as shown in Fig. 6.17. In order to go from (ω_1, ω_2) to (ω, ϕ) , we will first transform from the former coordinates to (Ω, θ) and then from (Ω, θ) to (ω, ϕ) . The rectangular coordinates (ω_1, ω_2) are related to the polar coordinates (Ω, θ) by (Fig. 6.17)

$$\Omega = \sqrt{\omega_1^2 + \omega_2^2} \quad (138)$$

$$\theta = \tan^{-1} \left(\frac{\omega_2}{\omega_1} \right). \quad (139)$$

In order to relate (Ω, θ) to (ω, ϕ) , we now introduce a new angle β , which is the angular position of a point (ω_1, ω_2) on arc OB in Fig. 6.17. Note from the figure that the point characterized by angle β is also characterized by parameter ω . The relationship between ω and β is given by

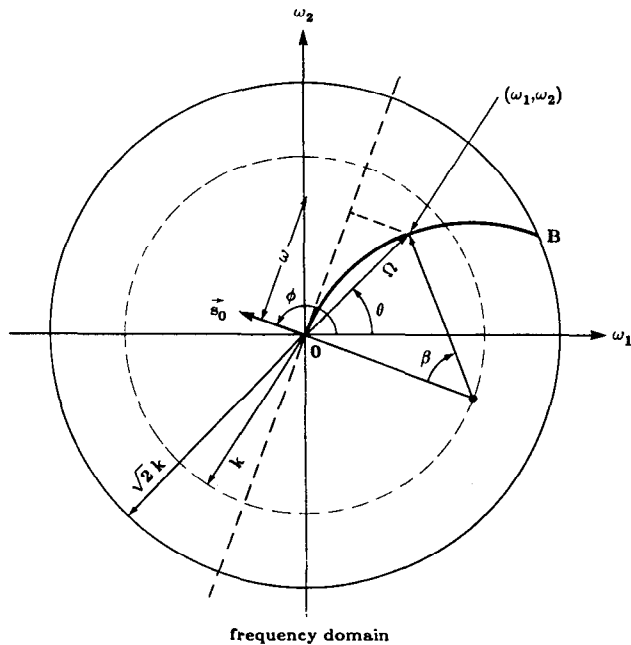
$$\omega = k \sin \beta. \quad (140)$$

The following relationship exists between the polar coordinates (Ω, θ) on the one hand and the parameters β and ϕ on the other:

Fig. 6.17: A second change of variables is used to relate the projection data to the object's Fourier transform. (From [Kak85] as modified from [Pan83].)

$$\beta = 2 \sin^{-1} \frac{\Omega}{2k} \quad (141)$$

$$\phi = \theta + \frac{\pi}{2} + \frac{\beta}{2}. \quad (142)$$



By substituting (141) in (140) and then using (138), we can express ω in terms of ω_1 and ω_2 . The result is shown below.

$$\omega = k \sin \left\{ 2 \sin^{-1} \left(\frac{\sqrt{\omega_1^2 + \omega_2^2}}{2k} \right) \right\}. \quad (143)$$

Similarly, by substituting (139) and (141) in (142), we obtain

$$\phi = \tan^{-1} \left(\frac{\omega_2}{\omega_1} \right) + \sin^{-1} \left(\frac{\sqrt{\omega_1^2 + \omega_2^2}}{2k} \right) + \frac{\pi}{2}. \quad (144)$$

These are our transformation equations for interpolating from the (ω, ϕ) parameters used for data representation to the (ω_1, ω_2) parameters needed for inverse transformation. To convert a particular rectangular point into (ω, ϕ) domain, we substitute its ω_1 and ω_2 values in (143) and (144). The resulting values for ω and ϕ may not correspond to any for which $Q(\omega, \phi)$ is known. By virtue of (137), $Q(\omega, \phi)$ will only be known over a uniformly sampled set of values for ω and ϕ . In order to determine Q at the calculated ω and ϕ , we use the following procedure. Given $N_\omega \times N_\phi$ uniformly located samples, $Q(\omega_i, \phi_j)$, we calculate a bilinearly interpolated value of this function at the desired ω and ϕ by using

$$Q(\omega, \phi) = \sum_{i=1}^{N_\omega} \sum_{j=1}^{N_\phi} Q(\omega_i, \phi_j) h_1(\omega - \omega_i) h_2(\phi - \phi_j), \quad (145)$$

where

$$h_1(\omega) = \begin{cases} 1 - \frac{|\omega|}{\Delta\omega} & |\omega| \leq \Delta\omega \\ 0 & \text{otherwise} \end{cases} \quad (146)$$

$$h_2(\phi) = \begin{cases} 1 - \frac{|\phi|}{\Delta\phi} & |\phi| \leq \Delta\phi \\ 0 & \text{otherwise;} \end{cases} \quad (147)$$

$\Delta\phi$ and $\Delta\omega$ are the sampling intervals for ϕ and ω , respectively. When expressed in the manner shown above, bilinear interpolation may be interpreted as the output of a filter whose impulse response is $h_1 h_2$.

The results obtained with bilinear interpolation can be considerably improved if we first increase the sampling density in the (ω, ϕ) -plane by using the computationally efficient method of zero-extending the two-dimensional inverse *fast Fourier transform* (FFT) of the $Q(\omega_i, \phi_j)$ matrix. The technique consists of first taking a two-dimensional inverse FFT of the $N_\omega \times N_\phi$ matrix consisting of the $Q(\omega_i, \phi_j)$ values, zero-extending the resulting $N_\omega \times N_\phi$

array of numbers to, let's say, $mN_\omega \times nM_\phi$, and then taking the FFT of this new array. The result is an mn -fold increase in the density of samples in the (ω, ϕ) -plane. After computing $Q(\omega, \phi)$ at each point of a rectangular grid by the procedure outlined above, the object $f(x, y)$ is obtained by a simple 2-D inverse FFT.

A different approach to frequency domain interpolation, called the unified frequency domain (UFR) interpolation, was proposed by Kaveh *et al.* [Kav84]. In this approach an interpolating function is derived by taking into account the object's spatial support. Consider an object's Fourier transform as might be measured in a diffraction tomography experiment. If the Fourier domain data are denoted by $F(u, v)$, then a reconstruction can be written

$$f(x, y) = i(x, y) \text{IFT} \{F(u, v)\} \quad (148)$$

where the indicator function is given by

$$i(x, y) = \begin{cases} 1 & \text{where the object is known to have support} \\ 0 & \text{elsewhere.} \end{cases} \quad (149)$$

If the Fourier transform of $i(x, y)$ is $I(u, v)$, then the spatially limited reconstruction can be rewritten

$$f(x, y) = \text{IFT} \{I(u, v) * F(u, v)\} \quad (150)$$

by noting that multiplication in the space domain is equivalent to convolution in the frequency domain. To perform the inverse Fourier transform fast it is necessary to have the Fourier domain data on a rectangular grid. First consider the frequency domain convolution; once the data are available on a rectangular grid the inverse Fourier transform can easily be calculated as it is for polynomial interpolation.

The frequency domain data for the UFR reconstruction can be written as

$$F(u, v) = \iint I(u - u', v - v') F(u', v') du' dv'. \quad (151)$$

Now recall that the experimental data, $F(u', v')$, are only available on the circular arcs in the $\phi - \omega$ space shown in Fig. 6.15. By using the change of variables

$$\begin{bmatrix} u' \\ v' \end{bmatrix} = \begin{bmatrix} T_1(\phi, \omega) \\ T_2(\phi, \omega) \end{bmatrix} = \begin{bmatrix} \cos \phi & -\sin \phi \\ \sin \phi & \cos \phi \end{bmatrix} \begin{bmatrix} \sqrt{k_0^2 - \omega^2} - k_0 \\ \omega \end{bmatrix} \quad (152)$$

and the Jacobian of the transformation given by

$$J(\phi, \omega) = \left| \frac{\partial(u', v')}{\partial(\phi, \omega)} \right| \quad (153)$$

the convolution can be rewritten

$$F(u, v) = \iint J(\phi, \omega) I(u - T_1(\phi, \omega), \\ v - T_2(\phi, \omega)) F(T_1(\phi, \omega), T_2(\phi, \omega)) d\phi d\omega. \quad (154)$$

This convolution integral gives us a means to get the frequency domain data on a rectangular grid and forms the heart of the UFR interpolation algorithm.

This integral can be easily discretized by replacing each integral with a summation over the projection angle, ϕ , and the spatial frequency of the received field, ω . The frequency domain data can now be written as

$$F(u, v) = \Delta_\phi \Delta_\omega \sum \sum J(\phi, \omega) \\ I(u - T_1(\phi, \omega), v - T_2(\phi, \omega)) \\ F(T_1(\phi, \omega), T_2(\phi, \omega)) \quad (155)$$

where Δ_ϕ and Δ_ω represent the sampling intervals in the $\phi - \omega$ space.

If the indicator function, $i(x, y)$, is taken to be 1 only within a circle of radius R , then its Fourier transform is written

$$I(u, v) = \frac{J_1(R\sqrt{u^2 + v^2})}{R\sqrt{u^2 + v^2}}. \quad (156)$$

A further simplification of this algorithm can be realized by noting that only the main lobe of the Bessel function will contribute much to the summation in (155). Thus a practical implementation can ignore all but the main lobe. This drastically reduces the computational complexity of the algorithm and leads to a reconstruction scheme that is only slightly more complicated than bilinear interpolation.

6.4.2 Backpropagation Algorithms

It has recently been shown by Devaney [Dev82] and Kaveh *et al.* [Kav82] that there is an alternative method for reconstructing images from the diffracted projection data. This procedure, called the *filtered backpropagation method*, is similar in spirit to the filtered backprojection technique of x-ray tomography. Unfortunately, whereas the filtered backprojection algorithms possess efficient implementations, the same can't be said for the filtered backpropagation algorithms. The latter class of algorithms is computationally intensive, much more so than the interpolation procedure discussed above. With regard to accuracy, they don't seem to possess any particular advantage especially if the interpolation is carried out after increasing the sampling density by the use of appropriate zero-padding as discussed above.

We will follow the derivation of the backpropagation algorithm as first

presented by Devaney [Dev82]. First consider the inverse Fourier transform of the object function,

$$o(\vec{r}) = \frac{1}{(2\pi)^2} \int_{-\infty}^{\infty} \int_{-\infty}^{\infty} O(\vec{K}) e^{j\vec{K} \cdot \vec{r}} d\vec{K}. \quad (157)$$

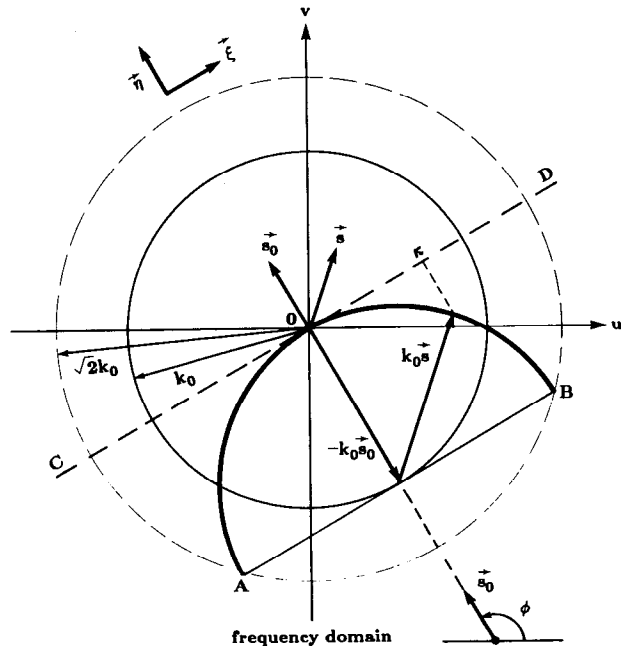
This integral most commonly represents the object function in terms of its Fourier transform in a rectangular coordinate system representing the frequency domain. As we have already discussed, a diffraction tomography experiment measures the Fourier transform of the object along circular arcs; thus it will be easier to perform the integration if we modify it slightly to use the projection data more naturally. We will use two coordinate transformations to do this: the first one will exchange the rectangular grid for a set of semicircular arcs and the second will map the arcs into their plane wave decomposition.

We first exchange the rectangular grid for semicircular arcs. To do this we represent $\vec{K} = (k_x, k_y)$ in (157) by the vector sum

$$\vec{K} = k_0(\vec{s} - \vec{s}_0) \quad (158)$$

where $\vec{s}_0 = (\cos \phi_0, \sin \phi_0)$ and $\vec{s} = (\cos \chi, \sin \chi)$ are unit vectors representing the direction of the wave vector for the transmitted and the received plane waves, respectively. This coordinate transformation is illustrated in Fig. 6.18.

Fig. 6.18: The $k_0\vec{r}_0$ and $k_0\vec{s}$ used in the backpropagation algorithm are shown here. (From [Pan83].)



To find the Jacobian of this transformation write

$$k_x = k_0 (\cos \chi - \cos \phi_0) \quad (159)$$

$$k_y = k_0 (\sin \chi - \sin \phi_0) \quad (160)$$

and

$$dk_x dk_y = |k_0^2 \sin(\chi - \phi_0)| d\chi d\phi_0 \quad (161)$$

$$= k_0 \sqrt{1 - \cos^2(\chi - \phi_0)} d\chi d\phi_0 \quad (162)$$

$$= k_0 \sqrt{1 - (\vec{s} \cdot \vec{s}_0)^2} d\chi d\phi_0 \quad (163)$$

and then (157) becomes

$$\begin{aligned} O(\vec{r}) &= \frac{1}{(2\pi)^2} \left(\frac{1}{2} \right) k_0^2 \\ &\cdot \int_0^{2\pi} \int_0^{2\pi} \sqrt{1 - (\vec{s} \cdot \vec{s}_0)^2} O[k_o(\vec{s} - \vec{s}_0)] e^{jk_0(\vec{s} - \vec{s}_0) \cdot \vec{r}} d\chi d\phi_0. \end{aligned} \quad (164)$$

The factor of 1/2 is necessary because as discussed in Section 6.4.1 the (χ, ϕ_0) coordinate system gives a double coverage of the (k_x, k_y) space.

This integral gives an expression for the scattered field as a function of the (χ, ϕ_0) coordinate system. The data that are collected will actually be a function of ϕ_0 , the projection angle, and κ , the one-dimensional frequency of the scattered field along the receiver line. To make the final coordinate transformation we take the angle χ to be relative to the (κ, γ) coordinate system. This is a more natural representation since the data available in a diffraction tomography experiment lie on a semicircle and therefore the data are available only for $0 \leq \chi \leq \pi$. We can rewrite the χ integral in (164) by noting

$$\cos \chi = \kappa/k_0 \quad (165)$$

$$\sin \chi = \gamma/k_0 \quad (166)$$

and therefore

$$d\chi = \frac{-1}{k_0 \gamma} d\kappa. \quad (167)$$

The χ integral becomes

$$\frac{1}{k_0} \int_{-\kappa_0}^{\kappa_0} \frac{d\kappa}{\gamma} |\kappa| O[k_0(\vec{s} - \vec{s}_0)] e^{jk_0(\vec{s} - \vec{s}_0) \cdot \vec{r}} d\kappa. \quad (168)$$

Using the Fourier Diffraction Theorem as represented by (104) we can approximate the Fourier transform of the object function, O , by a simple function of the first-order Born field, U_B , at the receiver line. Thus the object function in (168) can be written

$$O[k_0(\vec{s} - \vec{s}_0)] = -2\gamma j U_B(\kappa, \gamma - k_0) e^{-j\gamma l_0}. \quad (169)$$

In addition, if a rotated coordinate system is used for $\vec{r} = (\xi, \eta)$ where

$$\xi = x \sin \phi - y \cos \phi \quad (170)$$

and

$$\eta = x \cos \phi + y \sin \phi, \quad (171)$$

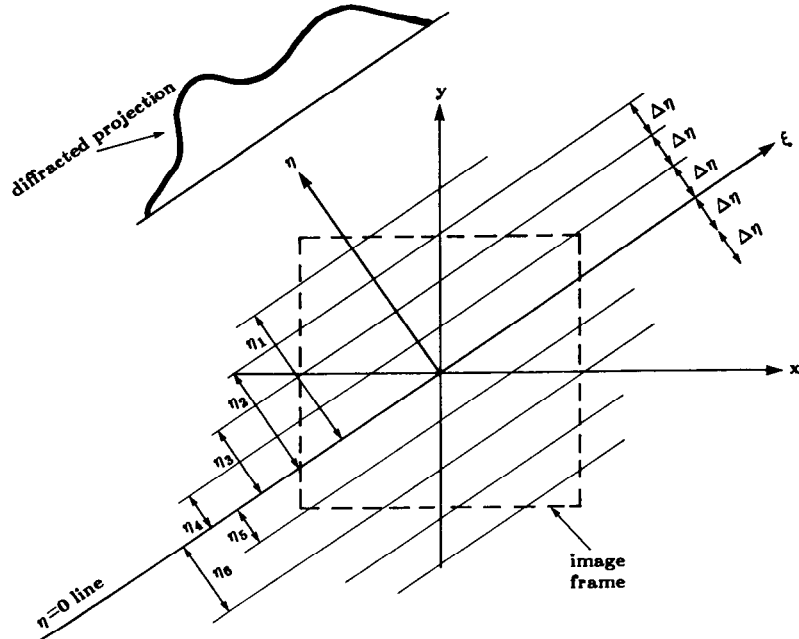
then the dot product $k_0(\vec{s} - \vec{s}_0)$ can be written

$$\kappa \xi + (\gamma - k_0) \eta. \quad (172)$$

Fig. 6.19: In backpropagation the projection is backprojected with a depth-dependent filter function. At each depth, η , the filter corresponds to propagating the field a distance of $\Delta\eta$. (From [Sla83].)

The coordinates (ξ, η) are illustrated in Fig. 6.19. Using the results above we can now write the χ integral of (164) as

$$\frac{2j}{k_0} \int_{-k_0}^{k_0} d\kappa |\kappa| U_B(\kappa, \gamma - k_0) e^{-j\gamma l_0} e^{\kappa \xi + (\gamma - k_0)\eta} \quad (173)$$



and the equation for the object function in (164) becomes

$$o(\vec{r}) = \frac{jk_0}{(2\pi)^2} \int_0^{2\pi} d\phi_0 \int_{-k_0}^{k_0} d\kappa |\kappa| U_B(\kappa, \gamma - k_0) e^{-j\gamma l_0} e^{j\kappa\xi + j(\gamma - k_0)\eta}. \quad (174)$$

To bring out the filtered backpropagation implementation, we write here separately the inner integration:

$$\Pi_\phi(\xi, \eta) = \frac{1}{2\pi} \int_{-\infty}^{\infty} \Gamma_\phi(\omega) H(\omega) G_\eta(\omega) \exp(j\omega\xi) d\omega \quad (175)$$

where

$$H(\omega) = |\omega|, \quad |\omega| \leq k_0, \quad (176)$$

$$= 0, \quad |\omega| > k_0 \quad (177)$$

$$G_\eta(\omega) = \exp[j(\sqrt{k_0^2 - \omega^2} - k_0)\eta], \quad |\omega| \leq k_0, \quad (178)$$

$$= 0, \quad |\omega| > k \quad (179)$$

and

$$\Gamma_\phi(\omega) = U_B(\kappa, \gamma - k_0) e^{-j\gamma l_0}. \quad (180)$$

Without the extra filter function $G_\eta(\omega)$, the rest of (175) would correspond to the filtering operation of the projection data in x-ray tomography. The filtering as called for by the transfer function $G_\eta(\omega)$ is depth dependent due to the parameter η , which is equal to $x \cos \phi + y \sin \phi$.

In terms of the filtered projections $\Pi_\phi(\xi, \eta)$ in (175), the reconstruction integral of (174) may be expressed as

$$f(x, y) = \frac{1}{2\pi} \int_0^{2\pi} d\phi \Pi_\phi(x \sin \phi - y \cos \phi, x \cos \phi + y \sin \phi). \quad (181)$$

The computational procedure for reconstructing an image on the basis of (175) and (181) may be presented in the form of the following steps:

Step 1: In accordance with (175), filter each projection with a separate filter for each depth in the image frame. For example, if we chose only nine depths as shown in Fig. 6.19, we would need to apply nine different filters to the diffracted projection shown there. (In most cases for a 128×128 reconstruction grid, the number of discrete depths chosen for filtering the projection will also be around 128. If there are much less than 128, spatial resolution will suffer.)

Step 2: To each pixel (x, y) in the image frame, in accordance with (181), allocate a value of the filtered projection that corresponds to the

nearest depth line. Since it is unlikely that a discrete implementation of (175) will lead to data at the precise location of each pixel, some form of polynomial interpolation (i.e., bilinear) will lead to better reconstructions.

Step 3: Repeat the preceding two steps for all projections. As a new projection is taken up, add its contribution to the current sum at pixel (x, y) .

The depth-dependent filtering in Step 1 makes this algorithm computationally very demanding. For example, if we choose N_η depth values, the processing of each projection will take $(N_\eta + 1)$ fast Fourier transforms (FFTs). If the total number of projections is N_ϕ , this translates into $(N_\eta + 1)N_\phi$ FFTs. For most $N \times N$ reconstructions, both N_η and N_ϕ will be approximately equal to N . Therefore, Devaney's filtered backpropagation algorithm will require approximately N^2 FFTs compared to $4N$ FFTs for frequency domain interpolation. (For precise comparisons, we must mention that the FFTs for the case of frequency domain interpolation are longer due to zero-padding.)

Devaney [Dev82] has also proposed a modified filtered backpropagation algorithm, in which $G_\eta(\omega)$ is simply replaced by a single $G_{\eta_0}(\omega)$ where $\eta_0 = x_0 \cos \phi + y_0 \sin \phi$, (x_0, y_0) being the coordinates of the point where local accuracy in reconstruction is desired. (Elimination of depth-dependent filtering reduces the number of FFTs to $2N_\phi$.)

6.5 Limitations

There are several factors that limit the accuracy of diffraction tomography reconstructions. These limitations are caused both by the approximations that must be made in the derivation of the reconstruction process and the experimental factors.

The mathematical and experimental effects limit the reconstruction in different ways. The most severe mathematical limitations are imposed by the Born and the Rytov approximations. These approximations are fundamental to the reconstruction process and limit the range of objects that can be examined. On the other hand, it is only possible to collect a finite amount of data and this gives rise to errors in the reconstruction which can be attributed to experimental limitations. Up to the limit in resolution caused by evanescent waves, and given a perfect reconstruction algorithm, it is possible to improve a reconstruction by collecting more data. It is important to understand the experimental limitations so that the experimental data can be used efficiently.

6.5.1 Mathematical Limitations

Computer simulations were performed to study several questions posed by diffraction tomography. In diffraction tomography there are different

approximations involved in the forward and inverse directions. In the forward process it is necessary to assume that the object is weakly scattering so that either the Born or the Rytov approximation can be used. Once an expression for the scattered field is derived it is necessary not only to measure the scattered fields but then numerically implement the inversion process.

By carefully designing the simulations it is possible to separate the effects of the approximations. To study the effects of the Born and the Rytov approximations it is necessary to calculate (or even measure) the exact fields and then use the best possible (most exact) reconstruction formulas available. The difference between the reconstruction and the actual object is a measure of the quality of the approximations.

6.5.2 Evaluation of the Born Approximation

The exact field for the scattered field from a cylinder, as shown by Weeks [Wee64] and by Morse and Ingard [Mor68], was calculated for cylinders of various sizes and refractive indexes. In the simulations that follow a single plane wave of unit wavelength was incident on the cylinder and the scattered field was measured along a line at a distance of 100 wavelengths from the origin. In addition, all refractive index changes were modeled as monopole scatterers. By doing this the directional dependence of dipole scatterers didn't have to be taken into account.

At the receiver line the received wave was measured at 512 points spaced at 1/2 wavelength intervals. In all cases the rotational symmetry of a single cylinder at the origin was used to reduce the computation time of the simulations.

The results shown in Fig. 6.20 are for cylinders of four different refractive indexes. In addition, Fig. 6.21 shows plots of the reconstructions along a line through the center of each cylinder. Notice that the y -coordinate of the center line is plotted in terms of change from unity.

The simulations were performed for refractive indexes that ranged from a 0.1% change (refractive index of 1.001) to a 20% change (refractive index of 1.2). For each refractive index, cylinders of size 1, 2, 4, and 10 wavelengths were reconstructed. This gives a range of phase changes across the cylinder (see (50)) from 0.004π to 16π .

Clearly, all the cylinders of refractive index 1.001 in Fig. 6.20 were perfectly reconstructed. As (50) predicts, the results get worse as the product of refractive index and radius gets larger. The largest refractive index that was successfully reconstructed was for the cylinder in Fig. 6.20 of radius 1 wavelength and a refractive index that differed by 20% from the surrounding medium.

While it is hard to evaluate quantitatively the two-dimensional reconstructions, it is certainly reasonable to conclude that only cylinders where the phase change across the object was less than or equal to 0.8π were adequately reconstructed. In general, the reconstruction for each cylinder where the

phase change across the cylinder was greater than π shows severe artifacts near the center. This limitation in the phase change across the cylinder is consistent with the condition expressed in (51).

Finally, it is important to note that the reconstructions in Fig. 6.20 don't show the most severe limitation of the Born approximation, which is that the real and imaginary parts of a reconstruction can get mixed up. For objects that don't satisfy the 0.8π phase change limitation the Born approximation causes some of the real energy in the reconstruction to be rotated into the imaginary plane. This further limits the use of the Born approximation when it is necessary to separately image the real and imaginary components of the refractive index.

6.5.3 Evaluation of the Rytov Approximation

Fig. 6.22 shows the simulated results for 16 reconstructions using the Rytov approximation. To emphasize the insensitivity of the Rytov approximation to large objects the largest object simulated had a diameter of 100λ . Note that these reconstructions are an improvement over those published in [Sla84] due to decreased errors in the phase unwrapping algorithm used.¹ This was accomplished by using an adaptive phase unwrapping algorithm as described in [Tri77] and by reducing the sampling interval on the receiver line to 0.125λ .

It should be pointed out that the rounded edges of the 1λ reconstructions aren't due to any limitation of the Rytov approximation but instead are the result of a two-dimensional low pass filtering of the reconstructions. Recall that for a transmission experiment an estimate of the object's Fourier transform is only available up to frequencies less than $\sqrt{2}k_0$. Thus the reconstructions shown in Fig. 6.22 show the limitations of both the Rytov approximation and the Fourier Diffraction Theorem.

6.5.4 Comparison of the Born and Rytov Approximations

Reconstructions using exact scattered data show the similarity of the Born and the Rytov approximations. Within the limits of the Fourier Diffraction Theorem the reconstructions in Figs. 6.20 and 6.22 of a 1λ object with a small refractive index are similar. In both cases the reconstructed change in refractive index is close to that of the simulated object.

The two approximations differ for objects that have a large refractive index change or have a large radius. The Born reconstructions are good at a large refractive index as long as the phase shift of the incident field as predicted by (50) is less than π .

On the other hand, the Rytov approximation is very sensitive to the refractive index but produces excellent reconstructions for objects as large as

¹ Many thanks to M. Kaveh of the University of Minnesota for pointing this out to the authors.

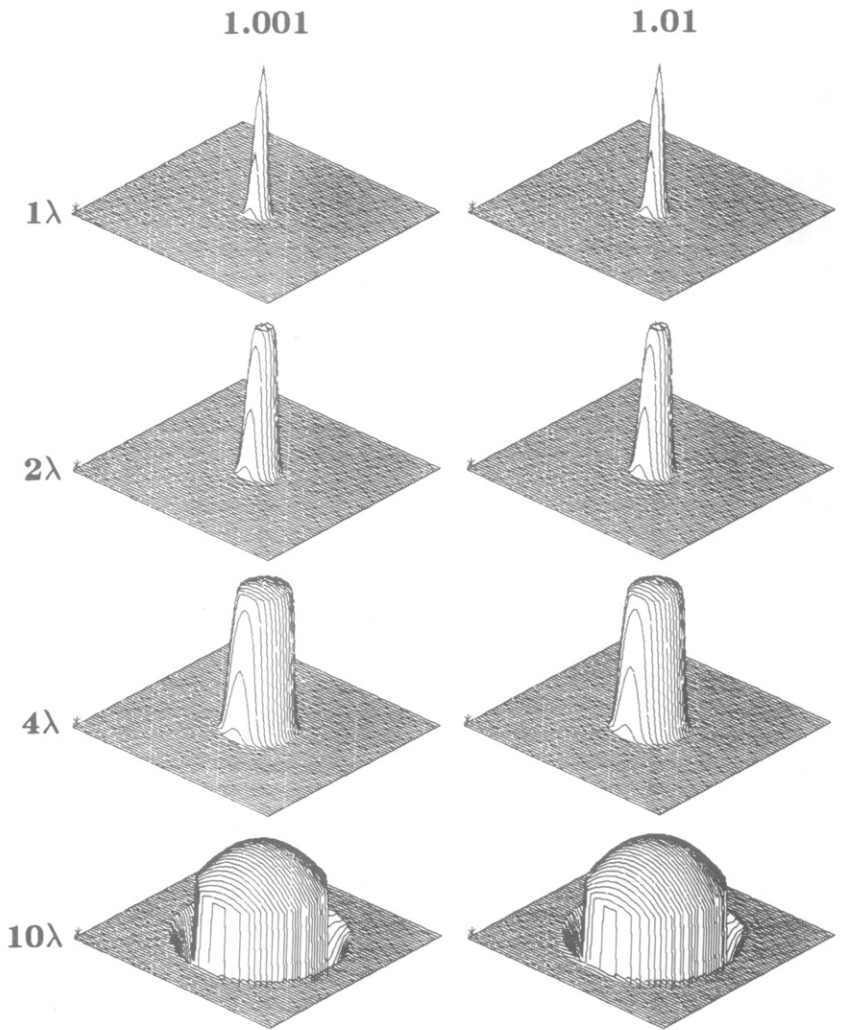


Fig. 6.20: Reconstructions of 16 different cylinders are shown indicating the effect of cylinder radius and refractive index on the Born approximation. (From [Sla84].)

100λ . Unfortunately, for objects with a refractive index larger than a few percent the Rytov approximation quickly deteriorates.

In addition to the qualitative studies a quantitative study of the error in the Born and Rytov reconstructions was also performed. As a measure of error we used the relative mean squared error in the reconstruction of the object function integrated over the entire plane. If the actual object function is $o(\vec{r})$ and the reconstructed object function is $o'(\vec{r})$, then the relative mean squared error (MSE) is

$$\iint \frac{[o(\vec{r}) - o'(\vec{r})]^2 d\vec{r}}{[o(\vec{r})]^2}. \quad (182)$$

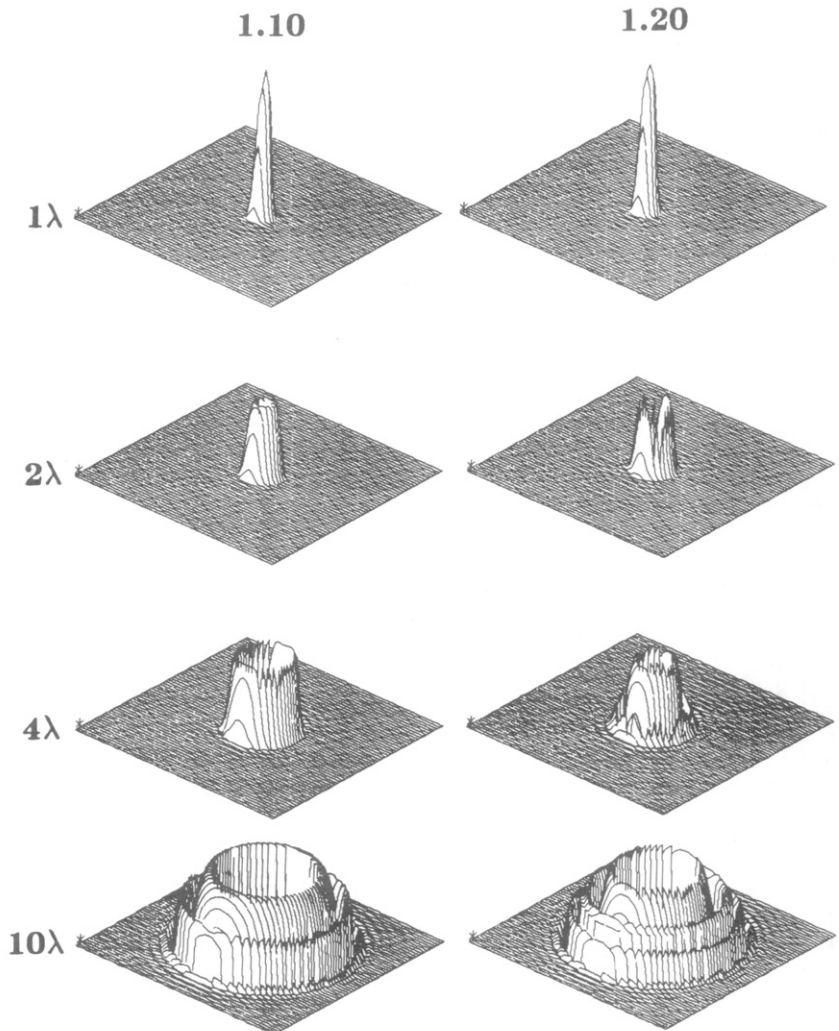


Fig. 6.20: *Continued.*

For this study 120 reconstructions were done of cylinders using the exact scattered data. In each case a 512-point receiver line was at a distance of 10λ from the center of the cylinder. Both the receiver line and the object reconstruction were sampled at $1/4\lambda$ intervals.

The plots of Fig. 6.23 present a summary of the mean squared error for cylinders of 1, 2, and 3λ in radius and for 20 refractive indexes between 1.01 and 1.20. In each case the error for the Born approximation is shown as a solid line while the Rytov reconstruction is shown as a broken line.

Many researchers [Kav82], [Kel69], [Sou83] have postulated that the Rytov approximation is superior to the Born but as the actual reconstructions in Fig. 6.23(a) show for a 1λ cylinder this is not necessarily true. While for

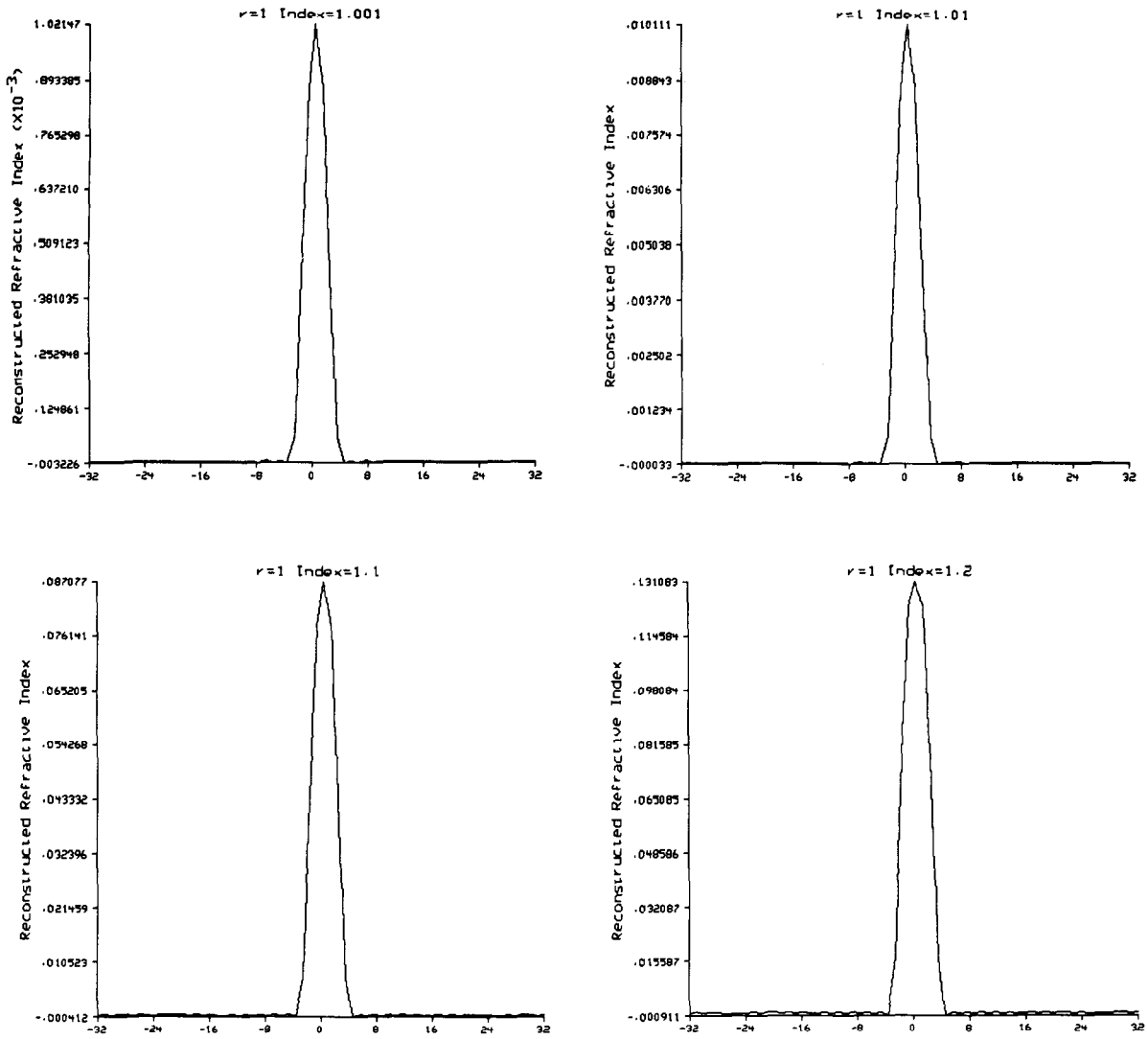


Fig. 6.21: Cross sections of the cylinders shown in Fig. 6.20 are shown here.

the cylinder of radius 2λ there is a region where the Rytov approximation shows less error than the Born reconstruction, this doesn't occur until the relative error is above 20%. What is clear is that both the Born and the Rytov approximations are only valid for small objects and that they both produce similar errors.

6.6 Evaluation of Reconstruction Algorithms

To study the approximations involved in the reconstruction process it is necessary to calculate scattered data assuming the forward approximations

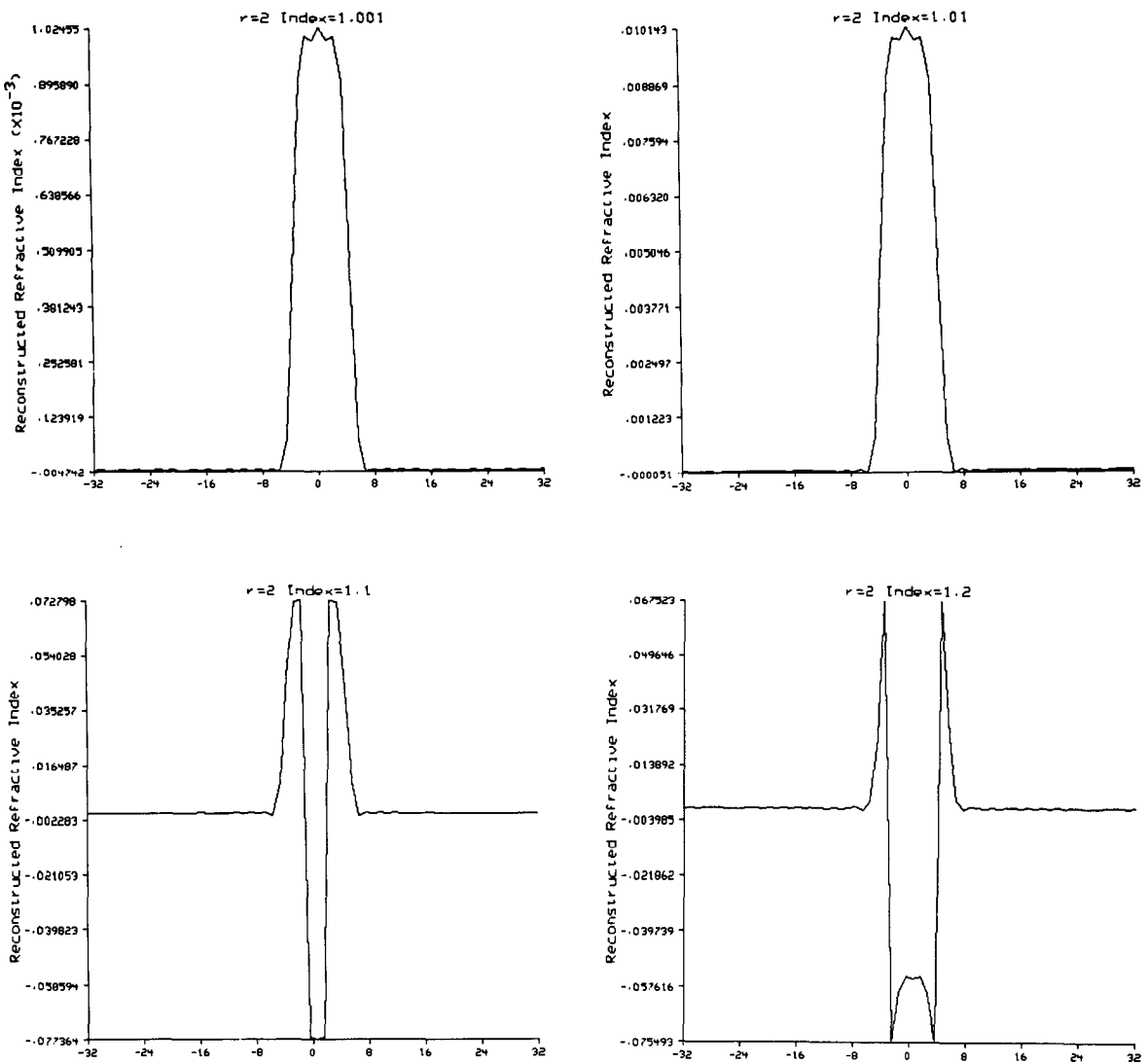


Fig. 6.21: *Continued.*

are valid. This can be done in one of two different ways. We have already discussed that the Born and Rytov approximations are valid for small objects and small changes in refractive index. Thus, if we calculate the exact scattered field for a small and weakly scattering object we can assume that either the Born or the Rytov approximation is exact.

A better approach is to recall the Fourier Diffraction Theorem, which says that the Fourier transform of the scattered field is proportional to the Fourier transform of the object along a semicircular arc. Since this theorem is the

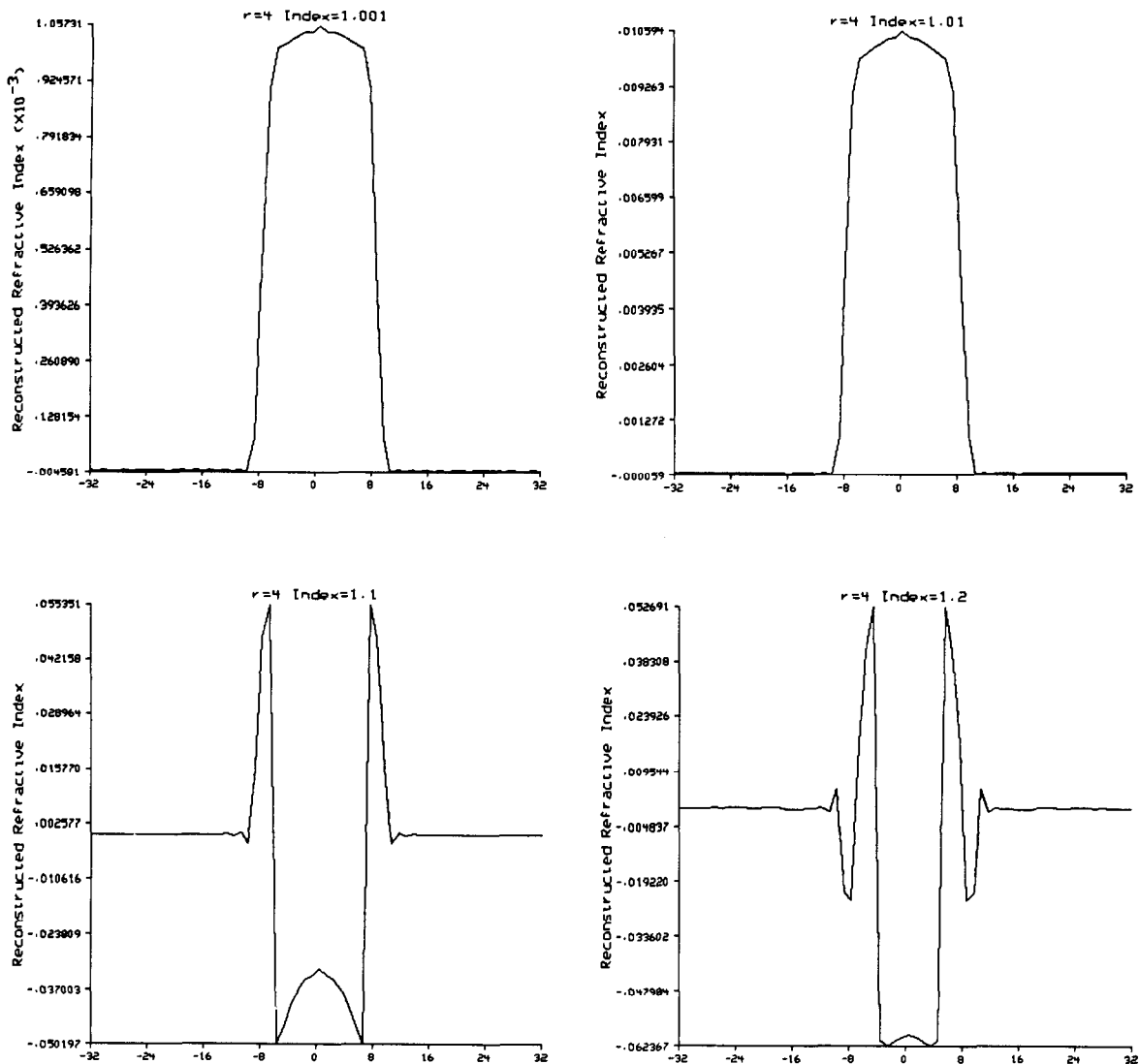


Fig. 6.21: *Continued.*

basis for our inversion algorithm, if we assume it is correct we can study the approximations involved in the reconstruction process.

If we assume that the Fourier Diffraction Theorem holds, the exact scattered field can be calculated exactly for objects that can be modeled as ellipses. The analytic expression for the Fourier transform of the object along an arc is proportional to the scattered fields. This procedure is fast and allows us to calculate scattered fields for testing reconstruction algorithms and experimental parameters.

To illustrate the accuracy of the interpolation-based algorithms, we will

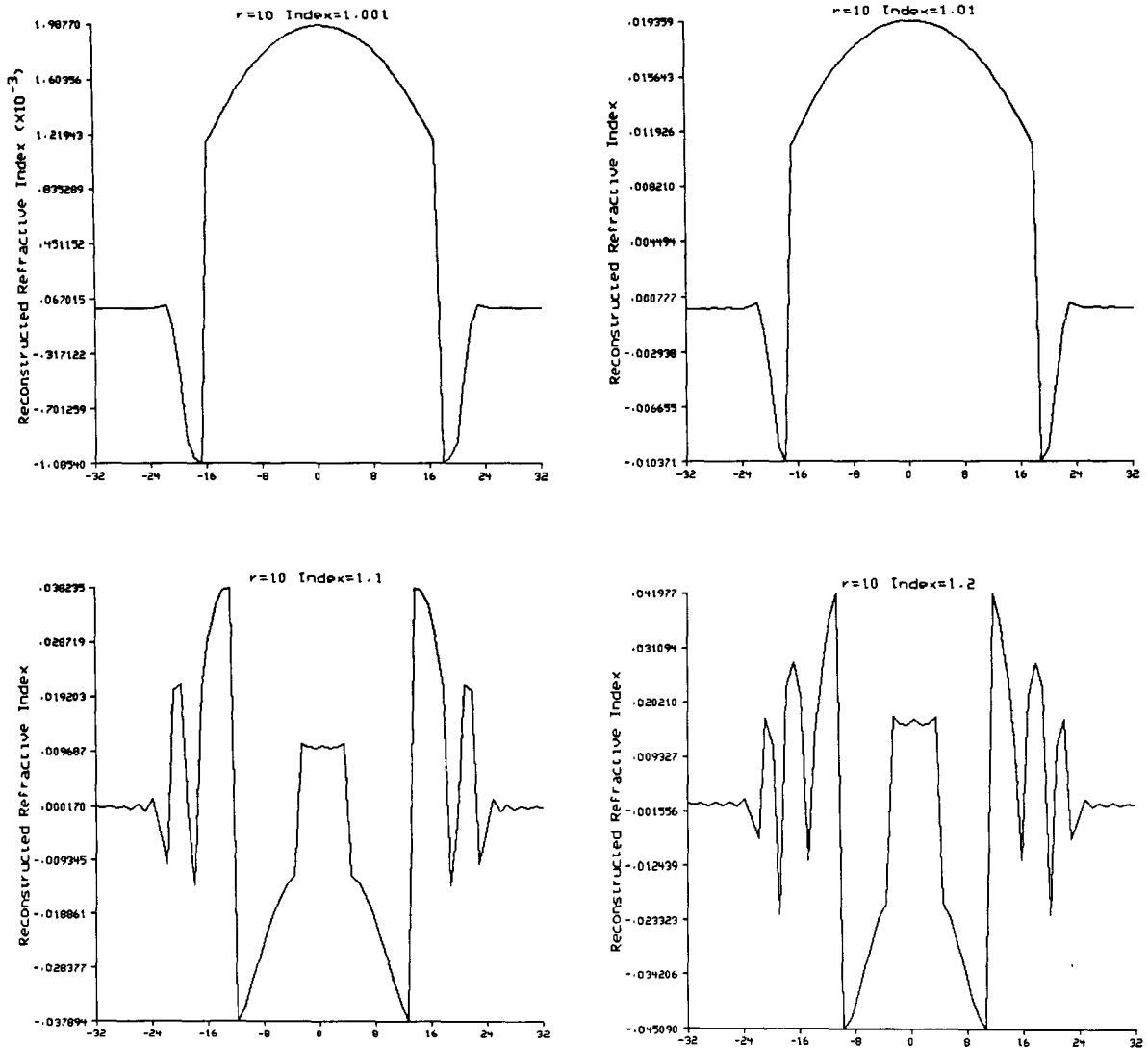


Fig. 6.21: *Continued.*

use the image in Fig. 6.24 as a test “object” for showing some computer simulation results. Fig. 6.24 is a modification of the Shepp and Logan “phantom” described in Chapter 3 to the case of diffraction imaging. The gray levels shown in Fig. 6.24 represent the refractive index values. This test image is a superposition of ellipses, with each ellipse being assigned a refractive index value as shown in Table 6.1.

A major advantage of using an image like that in Fig. 6.24 for computer simulation is that one can write analytical expressions for the transforms of the diffracted projections. The Fourier transform of an ellipse of semi-major

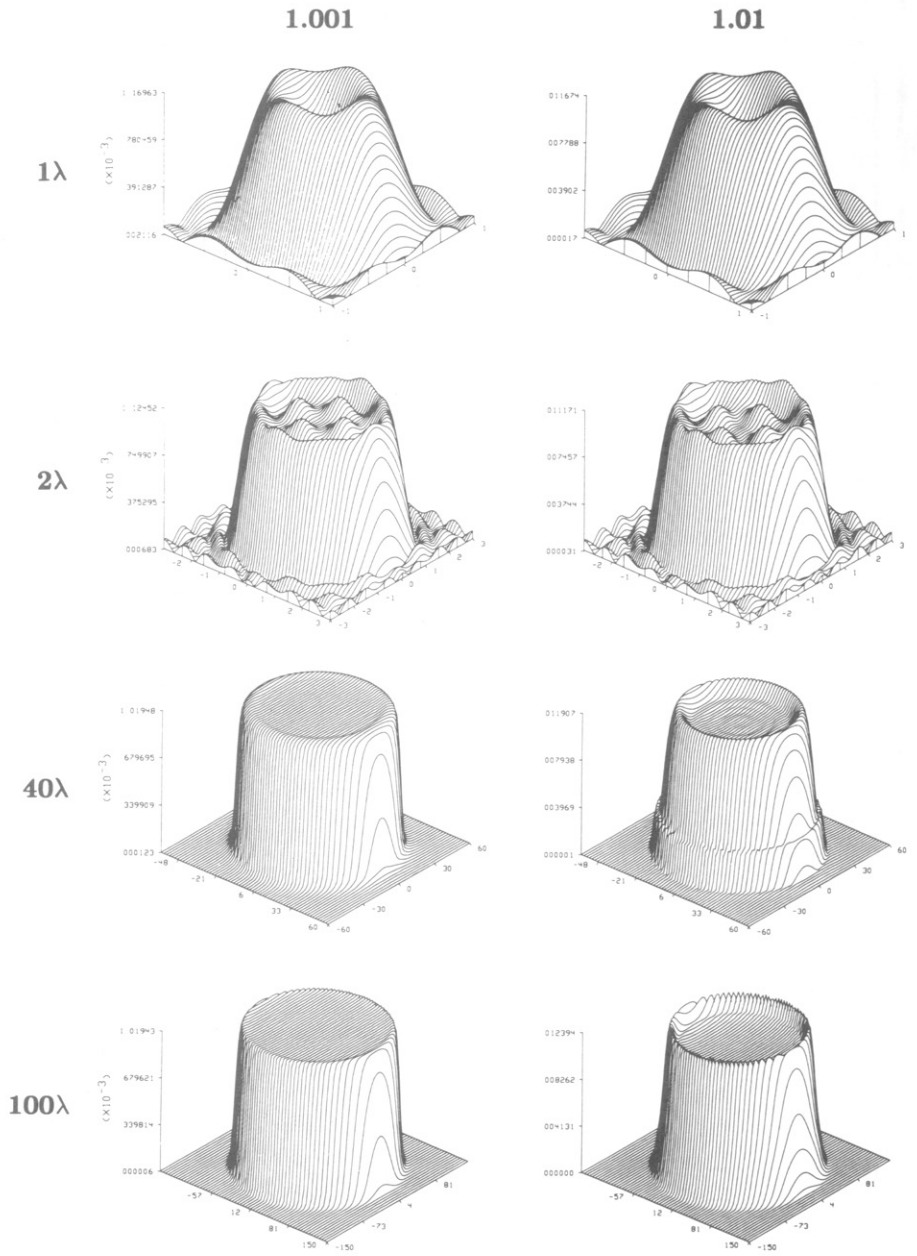


Fig. 6.22: Reconstructions of 16 different cylinders are shown indicating the effect of cylinder radius and refractive index on the Rytov approximation. These reconstructions were calculated by sampling the scattered fields at 16,384 points along a line 100λ from the edge of the object. A sampling interval of $6(R + 100)/16,384$ where R is the radius of the cylinder, was used to make it easier to unwrap the phase of the scattered fields. (Adapted from [Sla84].)

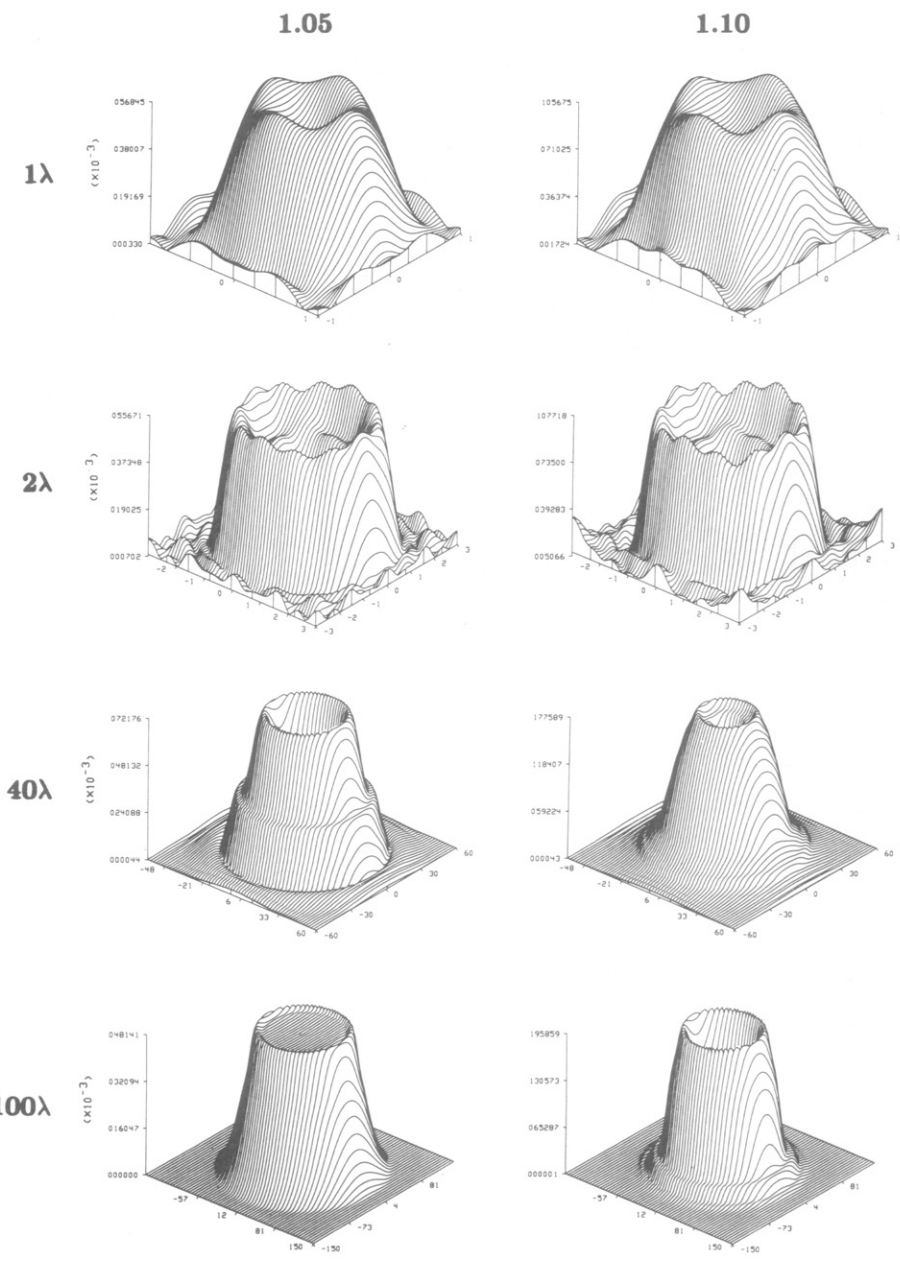


Fig. 6.22: *Continued.*

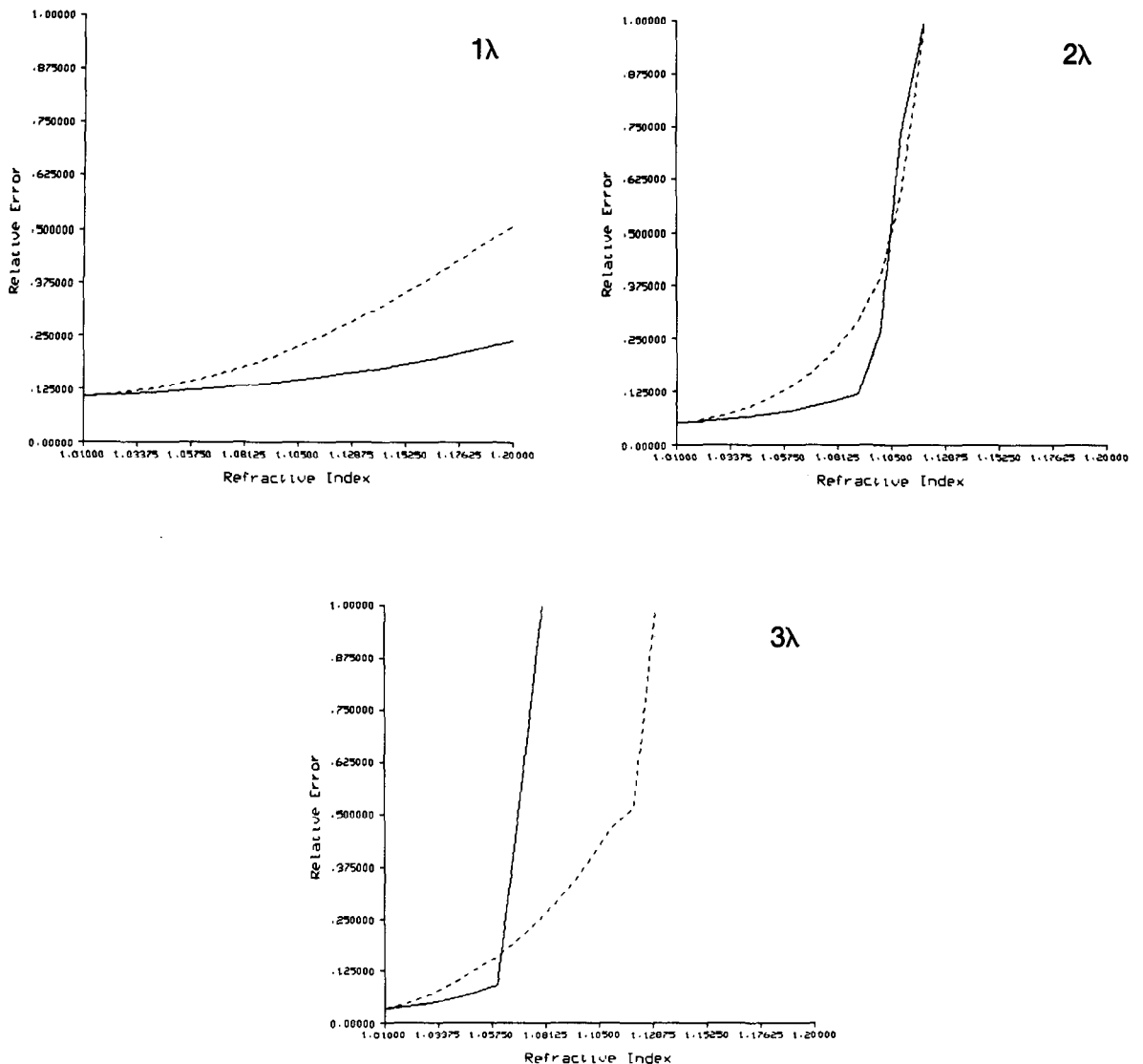


Fig. 6.23: The relative mean squared errors for reconstructions with the Born (solid) and the Rytov (broken) approximations are shown here. Each plot is a function of the refractive index of the cylinder. The mean squared error is plotted for cylinders of radius 1λ , 2λ , and 3λ . (From [Sla84].)

and semi-minor axes of lengths A and B , respectively, is given by

$$\frac{2\pi AJ_1[B\sqrt{(uA/B)^2 + v^2}]}{\sqrt{(uA/B)^2 + v^2}} \quad (183)$$

where u and v are spatial angular frequencies in the x and y directions, respectively, and J_1 is a Bessel function of the first kind and order 1. When the center of this ellipse is shifted to the point (x_1, y_1) , and the angle of the major axis tilted by α , as shown in Fig. 6.25(b), its Fourier transform

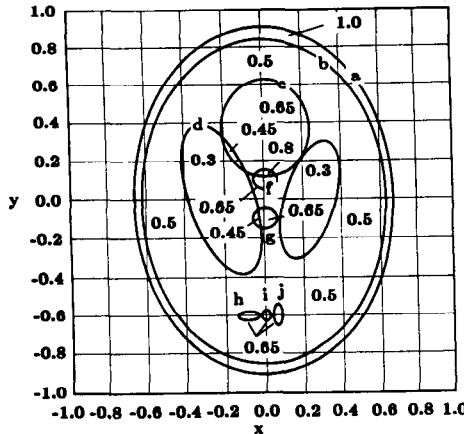


Fig. 6.24: For diffraction tomographic simulations a slightly modified version of the Shepp and Logan head phantom is used. (From [Pan83].)

becomes

$$e^{-j(ux_1 + vy_1)}$$

$$\cdot \frac{2\pi AJ_1\{B[((u \cos \alpha + v \sin \alpha)A/B)^2 + (-u \sin \alpha + v \cos \alpha)^2]^{1/2}\}}{[((u \cos \alpha + v \sin \alpha)A/B)^2 + (-u \sin \alpha + v \cos \alpha)^2]^{1/2}}.$$

(184)

Now consider the situation in which the ellipse is illuminated by a plane wave. By the Fourier Diffraction Theorem discussed previously, the Fourier transform of the transmitted wave fields measured on a line like TT' shown in Fig. 6.2(left), will be given by the values of the above function on a semicircular arc as shown in Fig. 6.2(right). If we assume weak scattering and therefore no interactions among the ellipses, the Fourier transform of the

Table 6.1: Summary of parameters for diffraction tomography simulations.

Center Coordinate	Major Axis	Minor Axis	Rotation Angle	Refractive Index
(0, 0)	0.92	0.69	90	1.0
(0, -0.0184)	0.874	0.6624	90	-0.5
(0.22, 0)	0.31	0.11	72	-0.2
(-0.22, 0)	0.41	0.16	108	-0.2
(0, 0.35)	0.25	0.21	90	0.1
(0, 0.1)	0.046	0.046	0	0.15
(0, -0.1)	0.046	0.046	0	0.15
(-0.08, -0.605)	0.046	0.023	0	0.15
(0, -0.605)	0.023	0.023	0	0.15
(0.06, -0.605)	0.046	0.023	90	0.15

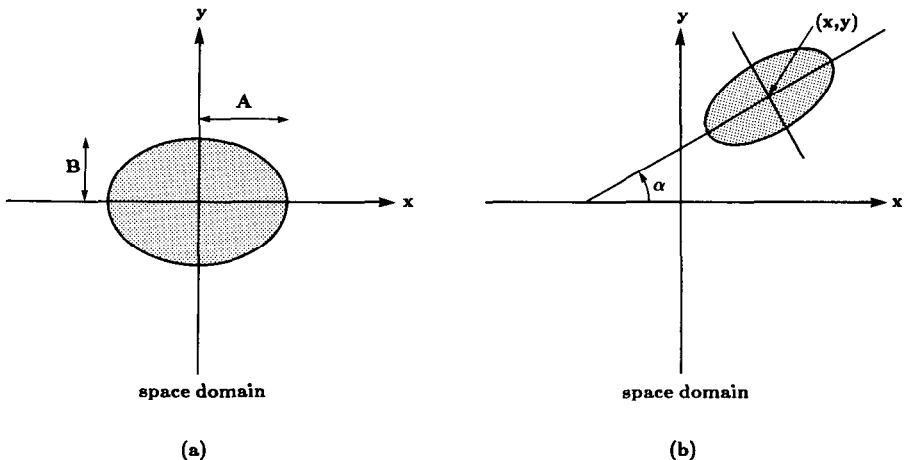


Fig. 6.25: Assuming the Fourier Slice Theorem, the field scattered by an ellipse can be easily calculated. (From [Kak85].)

total forward scattered field measured on the line TT' will be a sum of the values of functions like (184) over the semicircular arc. This procedure was used to generate the diffracted projection data for the test image.

We must mention that by generating the diffracted projection data for computer simulation by this procedure, we are only testing the accuracy of the reconstruction algorithm, without checking whether or not the “test object” satisfies the underlying assumption of weak scattering. In order to test this crucial assumption, we must generate exactly on a computer the forward scattered data of the object. For multicomponent objects, such as the one shown in Fig. 6.24, it is very difficult to do so due to the interactions between the components.

Pan and Kak [Pan83] presented the simulations shown in Fig. 6.26. Using a combination of increasing the sampling density by zero-padding the signal and bilinear interpolation, results were obtained in 2 minutes of CPU time on a VAX 11/780 minicomputer with a floating point accelerator (FPA). The reconstruction was done over a 128×128 grid using 64 views and 128 receiver positions. The number of operations required to carry out the interpolation and invert the object function is on the order of $N^2 \log N$. The resulting reconstruction is shown in Fig. 6.26(a).

Fig. 6.26(b) represents the result of backpropagating the data to 128 depths for each view, while Fig. 6.26(c) is the result of backpropagation to only a single depth centered near the three small ellipses at the bottom of the picture. The results were simulated on a VAX 11/780 minicomputer and the resulting reconstructions were done over a 128×128 grid. Like the previous image the input data consisted of 64 projections of 128 points each.

There was a significant difference in not only the reconstruction time but also the resulting quality. While the modified backpropagation only took 1.25 minutes, the resulting reconstruction is much poorer than that from the full backpropagation which took 30 minutes of CPU time. A comparison of the

various algorithms is shown in Table 6.2. Note that the table doesn't explicitly show the extra CPU time required if zero-padding is used in the frequency domain to make space domain interpolation easier. To a very rough approximation space domain interpolation and modified backpropagation algorithms take $N^2 \log N$ steps while the full backpropagation algorithm takes $N^3 \log N$ steps.

6.7 Experimental Limitations

In addition to the limits on the reconstructions imposed by the Born and the Rytov approximations, there are also the following experimental limitations to consider:

- Limitations caused by ignoring evanescent waves
- Sampling the data along the receiver line
- Finite receiver length
- Limited views of the object.

Each of the first three factors can be modeled as a simple constant low pass filtering of the scattered field. Because the reconstruction process is linear the net effect can be modeled by a single low pass filter with a cutoff at the lowest of the three cutoff frequencies. The experiment can be optimized by adjusting the parameters so that each low pass filter cuts off at the same frequency.

The effect of a limited number of views also can be modeled as a low pass filter. In this case, though, the cutoff frequency varies with the radial direction.

6.7.1 Evanescent Waves

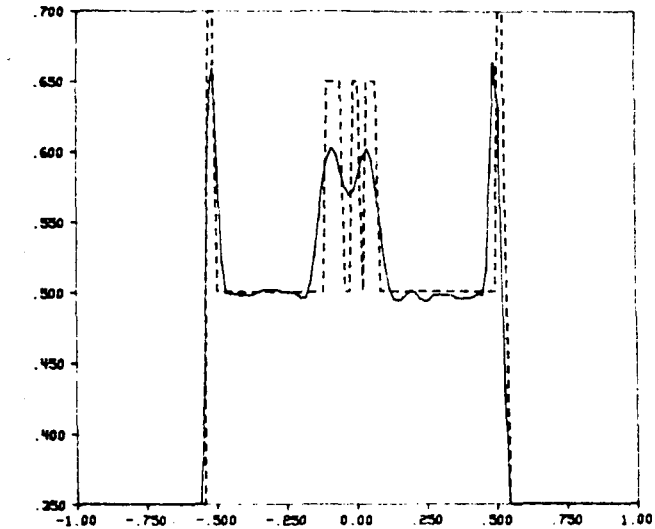
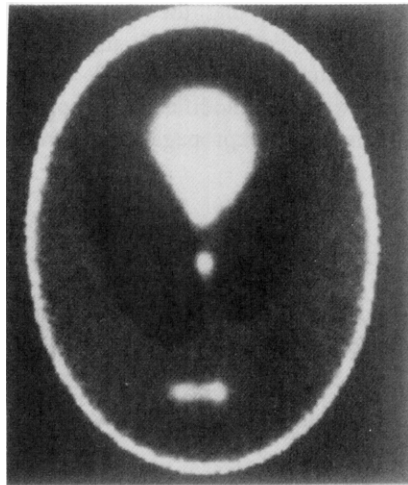
Since evanescent waves have a complex wavenumber they are severely attenuated over a distance of only a few wavelengths. This limits the highest received wavenumber to

$$k_{\max} = \frac{2\pi}{\lambda}. \quad (185)$$

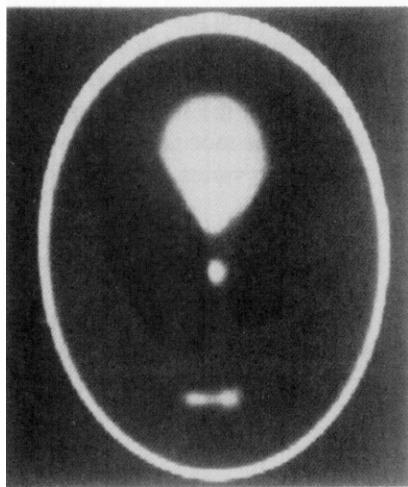
This is a fundamental limit of the propagation process and can only be improved by moving the experiment to a higher frequency (or shorter wavelength).

6.7.2 Sampling the Received Wave

After the wave has been scattered by the object and propagated to the receiver line, it must be measured. This is usually done with a point receiver.



(a)



(b)

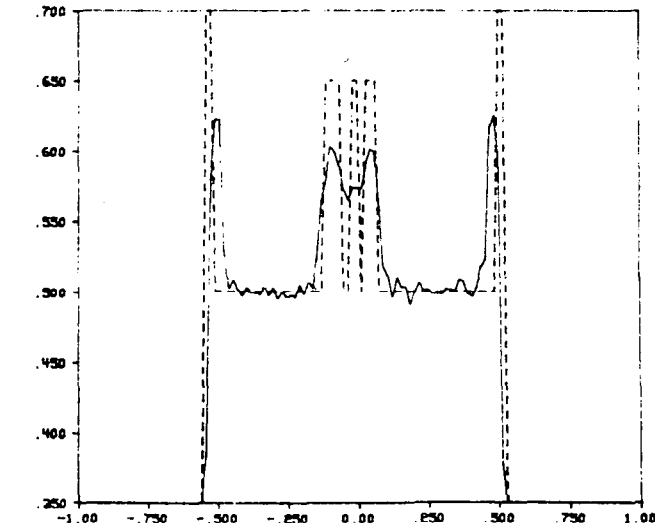
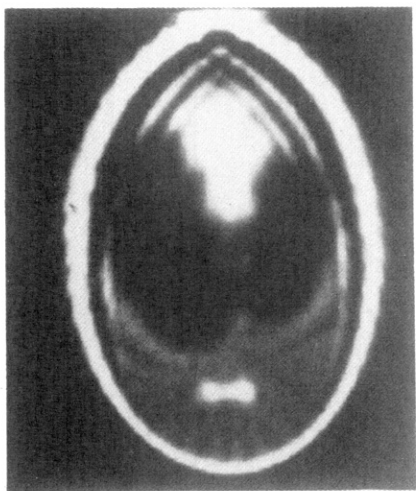


Fig. 6.26: The images show the results of using the (a) interpolation, (b) backpropagation, and (c) modified backpropagation algorithms on reconstruction quality. The solid lines of the graphs represent the reconstructed value along a line through the three ellipses at the bottom of the phantom. (From [Pan83].)

Unfortunately, it is not possible to sample at every point, so a nonzero sampling interval must be chosen. This introduces a measurement error into the process. By the Nyquist theorem this can be modeled as a low pass filtering operation, where the highest measured frequency is given by

$$k_{\text{meas}} = \frac{\pi}{T} \quad (186)$$

where T is the sampling interval.



(c)

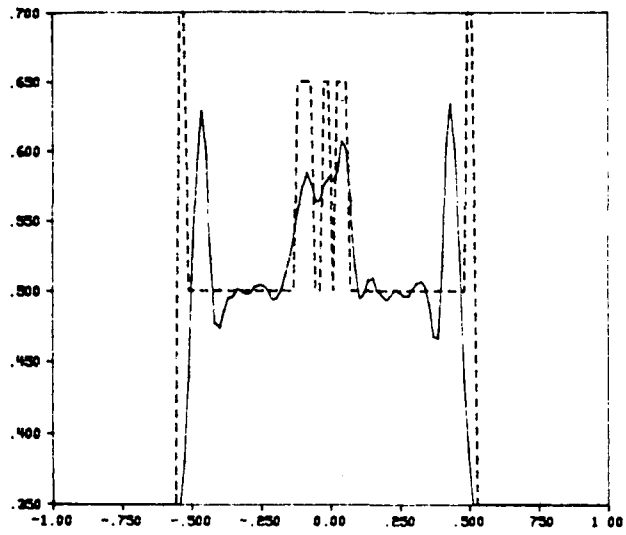


Fig. 6.26: *Continued.*

6.7.3 The Effects of a Finite Receiver Length

Not only are there physical limitations on the finest sampling interval but usually there is a limitation on the amount of data that can be collected. This generally means that samples of the received waveform will be collected at only a finite number of points along the receiver line. This is usually justified by taking data along a line long enough so that the unmeasured data can be safely ignored. Because of the wave propagation process this also introduces a low pass filtering of the received data.

Consider for a moment a single scatterer at some distance, l_0 , from the receiver line. The wave propagating from this single scatterer is a cylindrical wave in two dimensions or a spherical wave in three dimensions. This effect is diagrammed in Fig. 6.27. It is easy to see that the spatial frequencies vary with the position along the receiver line. This effect can be analyzed using two different approaches.

It is easier to analyze the effect by considering the expanding wave to be

Table 6.2: Comparison of algorithms.

Algorithm	Complexity	CPU Time (minutes)
Frequency Domain		
Interpolation	$N^2 \log N$	2
Backpropagation	$N_d N_\phi N \log N$	30
Modified Backpropagation	$N_\phi N \log N$	1.25

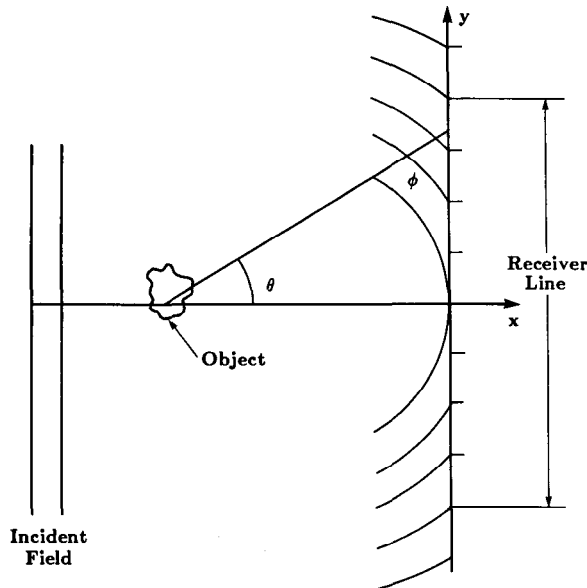


Fig. 6.27: An object scatters a field which is measured with a finite receiver line. (From [Sla83].)

locally planar at any point distant from the scatterer. At the point on the receiver line closest to the scatterer there is no spatial variation [Goo68]. This corresponds to receiving a plane wave or a received spatial frequency of zero.

Higher spatial frequencies are received at points along the receiver line that are farther from the origin. The received frequency is a function of the sine of the angle between the direction of propagation and a perpendicular to the receiver line. This function is given by

$$k(y) = k_{\max} \sin \theta \quad (187)$$

where θ is the angle and k_{\max} is the wavenumber of the incident wave. Thus at the origin, the angle, θ , is zero and the received frequency is zero. Only at infinity does the angle become equal to 90° and the received spatial frequency approach the theoretical maximum.

This reasoning can be justified on a more theoretical basis by considering the phase function of the propagating wave. The received wave at a point ($x = l_0, y$) due to a scatterer at the origin is given by

$$u(x = l_0, y) = \frac{e^{jk_0 \sqrt{x^2 + y^2}}}{\sqrt{x^2 + y^2}}. \quad (188)$$

The instantaneous spatial frequency along the receiver line (y varies) of this

wave can be found by taking the partial derivative of the phase with respect to y [Gag78].

$$\text{phase} = k_0 \sqrt{y^2 + x^2} \quad (189)$$

$$k_{\text{recv}} = \frac{k_0 y}{\sqrt{x^2 + y^2}} \quad (190)$$

where k_{recv} is the spatial frequency received at the point ($x = l_0$, y). From Fig. 6.27 it is easy to see that

$$\sin \theta = \frac{y}{\sqrt{x^2 + y^2}} \quad (191)$$

and therefore (187) and (190) are equivalent.

This relation, (190), can be inverted to give the length of the receiver line for a given maximum received frequency, k_{max} . This becomes

$$y = \pm \frac{k_{\text{max}} x}{\sqrt{k_0^2 - k_{\text{max}}^2}} . \quad (192)$$

Since the highest received frequency is a monotonically increasing function of the length of the receiver line, it is easy to see that by limiting the sampling of the received wave to a finite portion of the entire line a low passed version of the entire scattered wave will be measured. The highest measured frequency is a simple function of the distance of the receiver line from the scatterer and the length of measured data. This limitation can be better understood if the maximum received frequency is written as a function of the angle of view of the receiver line. Thus substituting

$$\tan \theta = \frac{y}{x} \quad (193)$$

we find

$$k_{\text{recv}} = \frac{k_0 (y/x)}{\sqrt{(y/x)^2 + 1^2}} \quad (194)$$

and

$$k_{\text{recv}} = \frac{k_0 \tan \theta}{\sqrt{\tan^2 \theta + 1}} . \quad (195)$$

Thus k_{recv} is a monotonically increasing function of the angle of view, θ . It is easy to see that the maximum received spatial frequency can be increased

either by moving the receiver line closer to the object or by increasing the length of the receiver line.

6.7.4 Evaluation of the Experimental Effects

The effect of a finite receiver length was simulated and results are shown in Fig. 6.28. The spatial frequency content of a wave, found by taking the FFT of the sampled points along the receiver line, was compared to the theoretical result as predicted by the Fourier transform of the object. The theory predicts that more of the high frequency components will be present as the length of the receiver line increases and this is confirmed by simulation.

While the above derivation only considered a single scatterer it is also approximately true for many scatterers collected at the origin. This is so because the inverse reconstruction process is linear and each point in the object scatters an independent cylindrical wave.

6.7.5 Optimization

Since each of the above three factors is independent of the other two, their effect in the frequency domain can be found by simply multiplying their frequency responses together. As has been described above, each of these effects can be modeled as a simple low pass filter so the combined effect is also a low pass filter but at the lowest frequency of the cutoff of the three effects.

First consider the effect of ignoring the evanescent waves. Since the maximum frequency of the received wave is limited by the propagation filter to

$$k_{\max} = \frac{2\pi}{\lambda}, \quad (196)$$

it is easy to combine this expression with the expression for the Nyquist frequency into a single expression for the smallest “interesting” sampling interval. This is given by

$$k_{\max} = k_{\text{meas}} \quad (197)$$

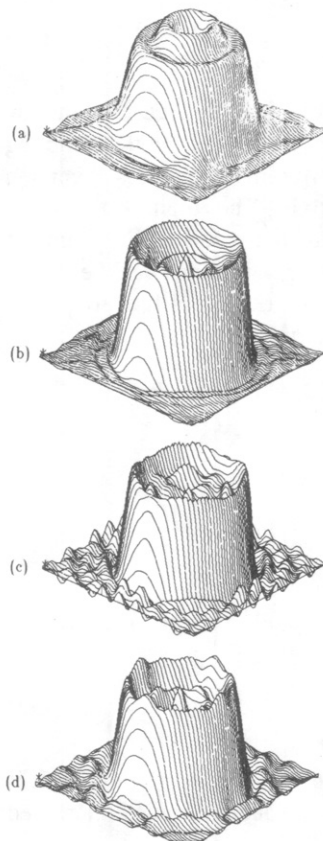
or

$$\frac{2\pi}{\lambda} = \frac{\pi}{T}. \quad (198)$$

Therefore,

$$T = \frac{\lambda}{2}. \quad (199)$$

Fig. 6.28: These four reconstructions show the effect of a finite receiver line. Reconstructions of an object using 64 detectors spaced at (a) 0.5λ , (b) 1.0λ , (c) 1.5λ , and (d) 2.0λ are shown here. (From [Sla83].)



If the received waveform is sampled with a sampling interval of more than $1/2$ wavelength, the measured data might not be a good estimate of the received waveform because of aliasing. On the other hand, it is not necessary to sample the received waveform any finer than $1/2$ wavelength since this provides no additional information. Therefore, we conclude that the sampling interval should be close to $1/2$ wavelength.

In general, the experiment will also be constrained by the number of data points (M) that can be measured along the receiver line. The distance from the object to the receiver line will be considered a constant in the derivation that follows. If the received waveform is sampled uniformly, the range of the receiver line is given uniquely by

$$y_{\max} = \pm \frac{MT}{2}. \quad (200)$$

This is also shown in Fig. 6.27.

For a receiver line at a fixed distance from the object and a fixed number of receiver points, the choice of T is determined by the following two competing considerations: As the sampling interval is increased the length of the receiver line increases and more of the received wave's high frequencies are measured. On the other hand, increasing the sampling interval lowers the maximum frequency that can be measured before aliasing occurs.

The optimum value of T can be found by setting the cutoff frequencies for the Nyquist frequency equal to the highest received frequency due to the finite receiver length and then solving for the sampling interval. If this constraint isn't met, then some of the information that is passed by one process will be attenuated by the others. This results in

$$\frac{\pi}{T} = \frac{k_0 y}{\sqrt{y^2 + x^2}} \quad (201)$$

evaluated at

$$k_0 = \frac{2\pi}{\lambda} \quad (202)$$

and

$$y = \frac{MT}{2}. \quad (203)$$

Solving for T^2 we find that the optimum value for T is given by

$$\left(\frac{T}{\lambda}\right)^2 = \frac{\sqrt{64(x/\lambda)^2 + M^2} + M}{8M}. \quad (204)$$

If we make the substitution

$$\alpha = \frac{x}{\lambda M} \quad (205)$$

we find that the optimum sampling interval is given by

$$\left(\frac{T}{\lambda} \right)^2 = \frac{\sqrt{64\alpha^2 + 1} + 1}{8}. \quad (206)$$

This formula is to be used with the constraint that the smallest positive value for the sampling interval is 1/2 wavelength.

The optimum sampling interval is confirmed by simulations. Again using the method described above for calculating the exact scattered fields, four simulations were made of an object of radius 10 wavelengths using a receiver line that was 100 wavelengths from the object. In each case the number of receiver positions was fixed at 64. The resulting reconstructions for sampling intervals of 0.05, 1, 1.5, and 2 wavelengths are shown in Fig. 6.28. Equation (206) predicts an optimum sampling interval of 1.3 wavelengths and this is confirmed by the simulations. The best reconstruction occurs with a sampling interval between 1 and 1.5 wavelengths.

6.7.6 Limited Views

In many applications it is not possible to generate or receive plane waves from all directions. The effect of this is to leave holes where there is no estimate of the Fourier transform of the object.

Since the ideal reconstruction algorithm produces an estimate of the Fourier transform of the object for all frequencies within a disk, a limited number of views introduces a selective filter for areas where there are no data. As shown by Devaney [Dev84] for the VSP case, a limited number of views degrades the reconstruction by low pass filtering the image in certain directions. Devaney's results are reproduced in Figs. 6.29 and 6.30.

6.8 Bibliographic Notes

The paper by Mueller *et al.* [Mue79] was responsible for focusing the interest of many researchers on the area of diffraction tomography, although from a purely scientific standpoint the technique can be traced back to the now classic paper by Wolf [Wol69] and a subsequent article by Iwata and Nagata [Iwa75].

The small perturbation approximations that are used for developing the diffraction tomography algorithms have been discussed by Ishimaru [Ish78] and Morse and Ingard [Mor68]. A discussion of the theory of the Born and the Rytov approximations was presented by Chernov in [Che60]. A

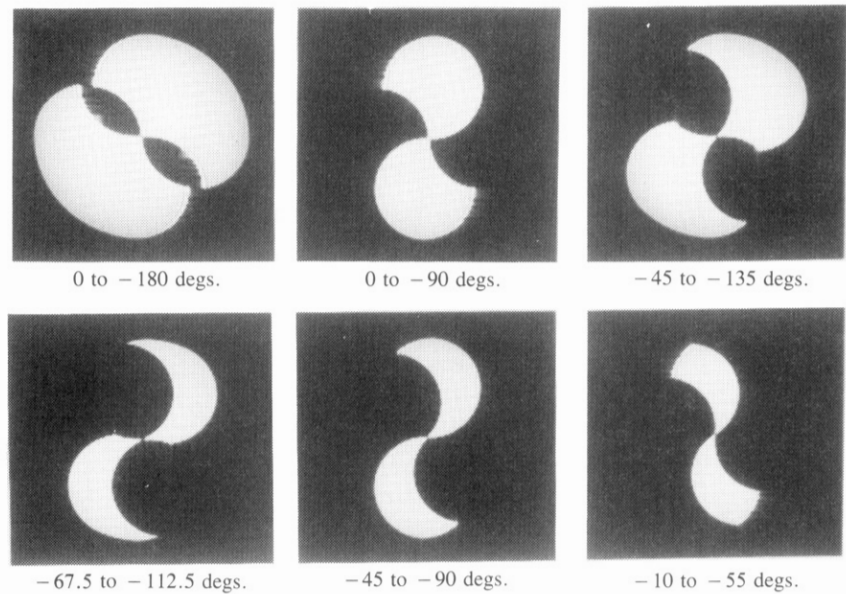


Fig. 6.29: These figures show the coverage in the frequency domain for six different angular receiver limitations. (From [Dev84].)

comparison of Born and Rytov approximations is presented in [Kel69], [Sla84], [Sou83]. The effect of multiple scattering on first-order diffraction tomography is described in [Azi83], [Azi85]. Another review of diffraction tomography is presented in [Kav86].

Diffraction tomography falls under the general subject of inverse scattering. The issues relating to the uniqueness and stability of inverse scattering solutions are addressed in [Bal78], [Dev78], [Nas81], [Sar81]. The mathematics of solving integral equations for inverse scattering problems is described in [Col83].

The filtered backpropagation algorithm for diffraction tomography was first advanced by Devaney [Dev82]. More recently, Pan and Kak [Pan83] showed that by using frequency domain interpolation followed by direct Fourier inversion, reconstructions of quality comparable to that produced by the filtered backpropagation algorithm can be obtained. Interpolation-based algorithms were first studied by Carter [Car70] and Mueller *et al.* [Mue80], [Sou84b]. An interpolation technique based on the known support of the object in the space domain is known as the unified frequency domain reconstruction (UFR) and is described in [Kav84]. Since the problems are related, the reader is referred to an excellent paper by Stark *et al.* [Sta81] that describes optimum interpolation techniques as applied to direct Fourier inversion of straight ray projections. The reader is also referred to [Fer79] to learn how in some cases it may be possible to avoid the interpolation, and still be able to reconstruct an object with direct 2-D Fourier inversion.

A diffraction tomography approach that requires only two rotational positions of the object has been advanced by Nahamoo *et al.* [Nah84] and

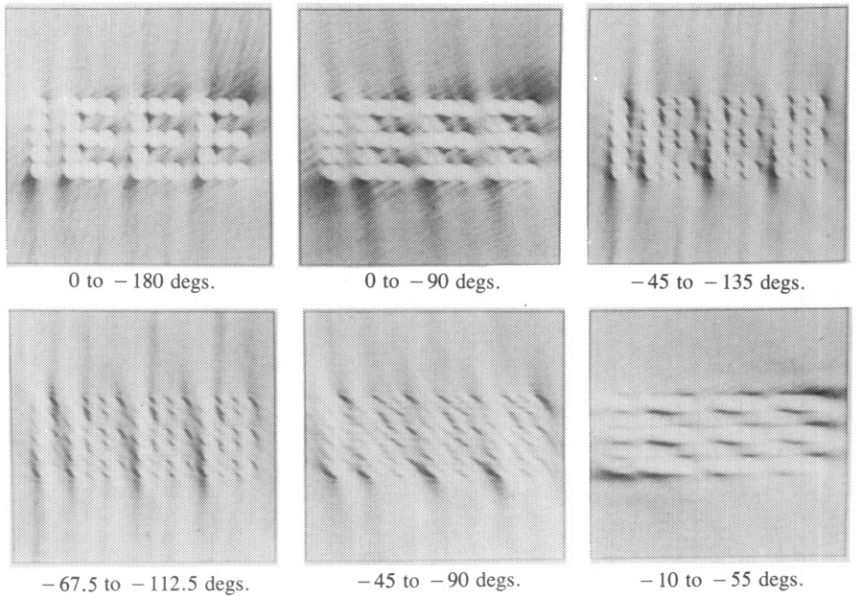


Fig. 6.30: *Images due to the limited field of views as shown in Fig. 6.29. (From [Dev84].)*

Devaney [Dev83], and its computer implementation has been studied by Pan and Kak [Pan83]. Diffraction tomography based on the reflected data has been studied in great detail by Norton and Linzer [Nor81].

The first experimental diffraction tomography work was done by Carter and Ho using optical energy and is described in [Car70], [Car74], [HoP76]. More recently, Kaveh and Soumekh have reported experimental results in [Kav80], [Kav81], [Kav82], [Sou83].

Finally, more accurate techniques for imaging objects that don't fall within the domain of the Born and Rytov approximations have been reported in [Joh83], [Tra83], [Sla85], [Bey84], [Bey85a], [Bey85b].

6.9 References

- [Azi83] M. Azimi and A. C. Kak, "Distortion in diffraction imaging caused by multiple scattering," *IEEE Trans. Med. Imaging*, vol. MI-2, pp. 176–195, Dec. 1983.
- [Azi85] ———, "Multiple scattering and attenuation phenomena in diffraction imaging," TR-EE 85-4, School of Electrical Engineering, Purdue Univ., Lafayette, IN, 1985.
- [Bal78] H. P. Baltes (Ed.), *Inverse Source Problems in Optics*. Berlin: Springer-Verlag, 1978.
- [Bar78] V. Barthes and G. Vasseur, "An inverse problem for electromagnetic prospection," in *Applied Inverse Problems*, P. C. Sabatier, Ed. Berlin: Springer-Verlag, 1978.
- [Bey84] G. Beylkin, "The inversion problem and applications of the generalized Radon transform," *Commun. Pure Appl. Math.*, vol. 37, pp. 579–599, 1984.

- [Bey85a] ——, “Imaging of discontinuities in the inverse scattering problem by inversion of a causal generalized Radon transform,” *J. Math. Phys.*, vol. 26-1, pp. 99–108, Jan. 1985.
- [Bey85b] G. Beylkin and M. L. Oristaglio, “Distorted-wave Born and distorted-wave Rytov approximations,” *Opt. Commun.*, vol. 53, pp. 213–216, Mar. 15, 1985.
- [Car70] W. H. Carter, “Computational reconstruction of scattering objects from holograms,” *J. Opt. Soc. Amer.*, vol. 60, pp. 306–314, Mar. 1970.
- [Car74] W. H. Carter and P. C. Ho, “Reconstruction of inhomogeneous scattering objects from holograms,” *Appl. Opt.*, vol. 13, pp. 162–172, Jan. 1974.
- [Che60] L. A. Chernov, *Wave Propagation in a Random Medium*. New York, NY: McGraw-Hill, 1960.
- [Col83] D. Colton and R. Kress, *Integral Equation Methods in Scattering Theory*. New York, NY: John Wiley and Sons, 1983.
- [Dev78] A. J. Devaney, “Nonuniqueness in the inverse scattering problem,” *J. Math. Phys.*, vol. 19, pp. 1525–1531, 1978.
- [Dev82] ——, “A filtered backpropagation algorithm for diffraction tomography,” *Ultrason. Imaging*, vol. 4, pp. 336–350, 1982.
- [Dev83] ——, “A computer simulation study of diffraction tomography,” *IEEE Trans. Biomed. Eng.*, vol. BME-30, pp. 377–386, July 1983.
- [Dev84] ——, “Geophysical diffraction tomography,” *IEEE Trans. Geological Science, Special Issue on Remote Sensing*, vol. GE-22, pp. 3–13, Jan. 1984.
- [Fer79] A. F. Fercher, H. Bartelt, H. Becker, and E. Wiltschko, “Image formation by inversion of scattered data: Experiments and computational simulation,” *Appl. Opt.*, vol. 18, pp. 2427–2439, 1979.
- [Gag78] R. Gagliardi, *Introduction to Communications Engineering*. New York, NY: John Wiley and Sons, 1978.
- [Goo68] J. W. Goodman, *Introduction to Fourier Optics*. San Francisco, CA: McGraw-Hill, 1968.
- [Gre78] J. F. Greenleaf, S. K. Kenue, B. Rajagopalan, R. C. Bahn, and S. A. Johnson, “Breast imaging by ultrasonic computer-assisted tomography,” in *Acoustical Imaging*, A. Metherell, Ed. New York, NY: Plenum Press, 1978.
- [Hoc73] H. Hochstadt, *Integral Equations*. New York, NY: John Wiley and Sons, 1973.
- [HoP76] P. C. Ho and W. H. Carter, “Structural measurement by inverse scattering in the first Born approximation,” *Appl. Opt.*, vol. 15, pp. 313–314, Feb. 1976.
- [Ish78] A. Ishimaru, *Wave Propagation and Scattering in Random Media*. New York, NY: Academic Press, 1978.
- [Iwa75] K. Iwata and R. Nagata, “Calculation of refractive index distribution from interferograms using the Born and Rytov’s approximations,” *Japan. J. Appl. Phys.*, vol. 14, pp. 1921–1927, 1975.
- [Joh83] S. A. Johnson and M. L. Tracy, “Inverse scattering solutions by a sinc basis, multiple source, moment method—Part I: Theory,” *Ultrason. Imaging*, vol. 5, pp. 361–375, 1983.
- [Kak85] A. C. Kak, “Tomographic imaging with diffracting and non-diffracting sources,” in *Array Signal Processing*, S. Haykin, Ed. Englewood Cliffs, NJ: Prentice-Hall, 1985.
- [Kav80] M. Kaveh, M. Soumekh, and R. K. Mueller, “Experimental results in ultrasonic diffraction tomography,” in *Acoustical Imaging*, vol. 9, K. Wang, Ed. New York, NY: Plenum Press, 1980, pp. 433–450.
- [Kav81] ——, “A comparison of Born and Rytov approximations in acoustic tomography,” in *Acoustical Imaging*, vol. 11, J. P. Powers, Ed. New York, NY: Plenum Press, 1981, pp. 325–335.
- [Kav82] ——, “Tomographic imaging via wave equation inversion,” in *Proc. Int. Conf. on Acoustics, Speech and Signal Processing*, May 1982, pp. 1553–1556.
- [Kav84] M. Kaveh, M. Soumekh, and J. F. Greenleaf, “Signal processing for diffraction tomography,” *IEEE Trans. Sonics Ultrason.*, vol. SU-31, pp. 230–239, July 1984.
- [Kav86] M. Kaveh and M. Soumekh, “Computer-assisted diffraction tomography,” in *Image Recovery, Theory and Applications*, H. Stark, Ed. New York, NY: Academic Press, 1986.

- [Kel69] J. B. Keller, "Accuracy and validity of the Born and Rytov approximations," *J. Opt. Soc. Amer.*, vol. 59, pp. 1003–1004, 1969.
- [Ken82] S. K. Kenue and J. F. Greenleaf, "Limited angle multifrequency diffraction tomography," *IEEE Trans. Sonics Ultrason.*, vol. SU-29, pp. 213–217, July 1982.
- [LuZ84] Z. Q. Lu, M. Kaveh, and R. K. Mueller, "Diffraction tomography using beam waves: Z-average reconstruction," *Ultrason. Imaging*, vol. 6, pp. 95–102, Jan. 1984.
- [McG82] R. McGowan and R. Kuc, "A direct relation between a signal time series and its unwrapped phase," *IEEE Trans. Acoust. Speech Signal Processing*, vol. ASSP-30, pp. 719–726, Oct. 1982.
- [Mor53] P. M. Morse and H. Feshbach, *Methods of Theoretical Physics*. New York, NY: McGraw-Hill, 1953.
- [Mor68] P. M. Morse and K. U. Ingard, *Theoretical Acoustics*. New York, NY: McGraw-Hill, 1968.
- [Mue79] R. K. Mueller, M. Kaveh, and G. Wade, "Reconstructive tomography and applications to ultrasonics," *Proc. IEEE*, vol. 67, pp. 567–587, 1979.
- [Mue80] R. K. Mueller, M. Kaveh, and R. D. Iverson, "A new approach to acoustic tomography using diffraction techniques," in *Acoustical Imaging*, A. Metherall, Ed. New York, NY: Plenum Press, 1980, pp. 615–628.
- [Nah81] D. Nahamoo, C. R. Crawford, and A. C. Kak, "Design constraints and reconstruction algorithms for transverse-continuous-rotate CT scanners," *IEEE Trans. Biomed. Eng.*, vol. BME-28, pp. 79–97, 1981.
- [Nah82] D. Nahamoo and A. C. Kak, "Ultrasonic diffraction imaging," TR-EE 82-20, School of Electrical Engineering, Purdue Univ., Lafayette, IN, 1982.
- [Nah84] D. Nahamoo, S. X. Pan, and A. C. Kak, "Synthetic aperture diffraction tomography and its interpolation-free computer implementation," *IEEE Trans. Sonics Ultrason.*, vol. SU-31, pp. 218–229, July 1984.
- [Nas81] M. Z. Nashed, "Operato-theoretic and computational approaches to illposed problems with application to antenna theory," *IEEE Trans. Antennas Propagat.*, vol. AP-29, pp. 220–231, 1981.
- [Nor81] S. J. Norton and M. Linzer, "Ultrasonic reflectivity imaging in three dimensions: Exact inverse scattering solutions for plane, cylindrical and spherical apertures," *IEEE Trans. Biomed. Eng.*, vol. BME-28, pp. 202–220, 1981.
- [OCo78] B. T. O'Connor and T. S. Huang, "Techniques for determining the stability of two-dimensional recursive filters and their application to image restoration," TR-EE 78-18, School of Electrical Engineering, Purdue Univ., Lafayette, IN, pp. 6–24, 1978.
- [Pan83] S. X. Pan and A. C. Kak, "A computational study of reconstruction algorithms for diffraction tomography: Interpolation vs. filtered-backpropagation," *IEEE Trans. Acoust. Speech Signal Processing*, vol. ASSP-31, pp. 1262–1275, Oct. 1983.
- [Sar81] T. K. Sarkar, D. D. Weiner, and V. K. Jain, "Some mathematical considerations in dealing with the inverse problem," *IEEE Trans. Antennas Propagat.*, vol. AP-29, pp. 373–379, 1981.
- [Sla83] M. Slaney and A. C. Kak, "Diffraction tomography," *Proc. S.P.I.E.*, vol. 413, pp. 2–19, Apr. 1983.
- [Sla84] M. Slaney, A. C. Kak, and L. E. Larsen, "Limitations of imaging with first order diffraction tomography," *IEEE Trans. Microwave Theory Tech.*, vol. MTT-32, pp. 860–873, Aug. 1984.
- [Sla85] M. Slaney and A. C. Kak, "Imaging with diffraction tomography," TR-EE 85-5, School of Electrical Engineering, Purdue Univ., Lafayette, IN, 1985.
- [Sou83] M. Soumekh, M. Kaveh, and R. K. Mueller, "Algorithms and experimental results in acoustic tomography using Rytov's approximation," in *Proc. Int. Conf. on Acoustics, Speech and Signal Processing*, Apr. 1983, pp. 135–138.
- [Sou84a] ——, "Fourier domain reconstruction methods with application to diffraction tomography," in *Acoustical Imaging*, vol. 13, M. Kaveh, R. K. Mueller, and J. F. Greenleaf, Eds. New York, NY: Plenum Press, 1984, pp. 17–30.
- [Sou84b] M. Soumekh and M. Kaveh, "Image reconstruction from frequency domain data on arbitrary contours," in *Proc. Conf. on Acoustics, Speech and Signal Processing*, 1984, pp. 12A.2.1–12A.2.4.
- [Sta81] H. Stark, J. W. Woods, I. Paul, and R. Hingorani, "Direct Fourier reconstruction in

- computer tomography," *IEEE Trans. Acoust. Speech Signal Processing*, vol. ASSP-29, pp. 237–244, 1981.
- [Tra83] M. L. Tracy and S. A. Johnson, "Inverse scattering solutions by a sinc basis, multiple source, moment method—Part II: Numerical evaluations," *Ultrason. Imaging*, vol. 5, pp. 376–392, 1983.
- [Tri77] J. M. Trbolet, "A new phase unwrapping algorithm," *IEEE Trans. Acoust. Speech Signal Processing*, vol. ASSP-25, pp. 170–177, Apr. 1977.
- [Wee64] W. L. Weeks, *Electromagnetic Theory for Engineering Applications*. New York, NY: John Wiley and Sons, Inc., 1964.
- [Wol69] E. Wolf, "Three-dimensional structure determination of semitransparent objects from holographic data," *Opt. Commun.*, vol. 1, pp. 153–156, 1969.